Low-boiling-point perfluorocarbon nanodroplets for adaptable ultrasound-induced blood-brain barrier opening

Ambre Dauba, Claire Spitzlei, Kathlyne Jayne B Bautista, Laurène Jourdain, Erwan Selingue, Kelly E Vantreeck, Jacob A Mattern, Caroline Denis, Malika Ouldali, Ana-Andreea Arteni, et al.

Journal of Controlled Release 376 (2024) 441–456

Contents lists available at ScienceDirect

Journal of Controlled Release

journal homepage: www.elsevier.com/locate/jconrel

Low-boiling-point perfluorocarbon nanodroplets for adaptable ultrasound-induced blood-brain barrier opening

Ambre Dauba [a], Claire Spitzlei [a,b], Kathlyne Jayne B. Bautista [c], Laurène Jourdain [a], Erwan Selingue [d], Kelly E. VanTreeck [c,g], Jacob A. Mattern [c,g], Caroline Denis [a], Malika Ouldali [e], Ana-Andreea Arteni [e], Charles Truillet [a], Benoit Larrat [d], James Tsuruta [c], Phillip G. Durham [c], Virginie Papadopoulou [c,f], Paul A. Dayton [c], Nicolas Tsapis [b,*], Anthony Novell [a,*]

[a] Université Paris-Saclay, CEA, CNRS, Inserm, BioMaps, SHFJ, Orsay 91401, France
[b] Université Paris-Saclay, CNRS, Institut Galien Paris-Saclay, 91400 Orsay, France
[c] Joint Department of Biomedical Engineering, The University of North Carolina at Chapel Hill, North Carolina State University, Chapel Hill, North Carolina, USA
[d] Université Paris-Saclay, CEA, CNRS, Baobab, NeuroSpin, Gif-sur-Yvette 91191, France
[e] Université Paris-Saclay, CEA, CNRS, Institute for Integrative Biology of the Cell (I2BC), Cryo-electron Microscopy Facility, CRYOEM-Gif, 91198 Gif-sur-Yvette, France
[f] Department of Radiology, The University of North Carolina at Chapel Hill, Chapel Hill, North Carolina, USA
[g] Division of Pharmacoengineering and Molecular Pharmaceutics, Eshelman School of Pharmacy, The University of North Carolina at Chapel Hill, Chapel Hill, NC 27599, USA

ARTICLE INFO

Keywords:
Blood-brain barrier
Focused ultrasound
Nanodroplets
Perfluorocarbon
Drug delivery

ABSTRACT

Low-boiling point perfluorocarbon nanodroplets (NDs) are valued as effective sonosensitive agents, encapsulating a liquid perfluorocarbon that would instantaneously vaporize at body temperature without the NDs shell. Those NDs have been explored for both therapeutic and diagnostic purposes. Here, phospholipid-shelled nanodroplets containing octafluoropropane (C_3F_8) or decafluorobutane (C_4F_{10}) formed by condensation of microbubbles were thoroughly characterized before blood-brain (BBB) permeabilization. Transmission electron microscopy (TEM) and cryo-TEM were employed to confirm droplet formation while providing high-resolution insights into the droplet surface and lipid arrangement assessed from electron density observation after condensation. The vaporization threshold of NDs was determined with a high-speed camera, and the frequency signal emitted by the freshly vaporized bubbles was analyzed using cavitation detection. C_3F_8 NDs exhibited vaporization at 0.3 MPa ($f_0 = 1.5$ MHz, 50 cycles), and emitted signals at 2 f_0 and 1.5 f_0 from 0.45 MPa onwards ($f_0 = 1.5$ MHz, 50 cycles), while broadband noise was measured starting from 0.55 MPa. NDs with the higher boiling point C_4F_{10} vaporized at 1.15 MPa and emitted signals at 2 f_0 from 0.65 MPa and 1.5 f_0 from 0.9 MPa, while broadband noise was detected starting from 0.95 MPa. Both ND formulations were used to permeabilize the BBB in healthy mice using tailored ultrasound sequences, allowing for the identification of optimal applications for each NDs type. C_3F_8 NDs proved suitable and safe for permeabilizing a large area, potentially the entire brain, at low acoustic pressure. Meanwhile, C_4F_{10} droplets facilitated very localized (400 μm isotropic) permeabilization at higher pressure. This study prompts a closer examination of the structural rearrangements occurring during the condensation of microbubbles into NDs and highlights the potential to tailor solutions for different brain pathologies by choosing the composition of the NDs and adjusting the ultrasound sequence.

Abbreviations: ADV, acoustic droplet vaporization; AUC, area under the curve; AUCR, AUC ratio; BBB, blood-brain barrier; C_3F_8, octafluoropropane; C_4F_{10}, decafluorobutane; DSPC, 1,2-distearoyl-sn-glycero-3-phosphocholine; DSPE-PEG2000, 1,2-distearoyl-*sn*-glycero-3-phosphoethanolamine-N-[methoxy(polyethylene glycol)-2000]; FUS, focused ultrasound; MI, mechanical index; MRI, magnetic resonance imaging; NDs, nanodroplets; NTA, nanoparticle tracking analysis; PBS, phosphate bufferred saline; PCCA, phase-change contrast agents; PNP, peak negative pressure; PRF, pulse repetition frequency; SPOS, single-particle optical sizing; TEM, transmission electron microscopy.

* Corresponding authors.
E-mail addresses: nicolas.tsapis@universite-paris-saclay.fr (N. Tsapis), anthony.novell@universite-paris-saclay.fr (A. Novell).

https://doi.org/10.1016/j.jconrel.2024.10.023
Received 26 June 2024; Received in revised form 11 October 2024; Accepted 14 October 2024
Available online 23 October 2024

1. Introduction

The blood-brain barrier (BBB) serves as a protective and regulatory physiological barrier for the central nervous system [1]. Despite safeguarding against potentially harmful substances, the BBB poses a significant challenge for the intracerebral penetration of nearly all pharmaceuticals designed for brain disease treatment [2]. Among the different methods for transporting drugs through the BBB, the combination of focused ultrasound (FUS) with microbubbles stands out [3], given its targeted, reversible and non-invasive nature [4]. This technique has demonstrated enhanced drug delivery to the central nervous system [5] while showing the ability to restore physiological function within a few hours after BBB opening [2]. The procedure is currently undergoing clinical evaluation, mainly for the treatment of glioblastoma [6,7], and Alzheimer's [8] among other brain pathologies.

When exposed to low-intensity ultrasound, microbubbles undergo symmetrical oscillations, where their expansion and compression are inversely related to the local ultrasound pressure [9]. By increasing the acoustic pressure of the ultrasonic wave, the oscillations of the bubble become non-linear, with an extended expansion phase due to their greater resistance to compression compared to expansion [9]. This regime is called stable cavitation. At a certain point of increasing pressure, microbubble enter the inertial cavitation regime where the oscillation amplitude can grow rapidly until the microbubble collapse [9,10]. Stable cavitation is the preferable state for safely opening the BBB [11]. By contrast, inertial cavitation results in the collapse of microbubbles accompanied by various intense physical phenomena such as micro-jets, microbubble fragmentation, and the generation of shock waves that may damage the vascular endothelium [9,12,13]. To be used for BBB opening, bubbles must possess the following characteristics: (i) high compressibility to oscillate in response to ultrasound, (ii) stability to circulate long enough to perform their purpose, and (iii) low toxicity [14].

The most commonly employed sonosensitive agents for BBB opening using FUS are phospholipid-shelled microbubbles. Microbubble diameter is typically between 1 and 10 μm [15]. However, their ability to open the BBB is limited by their poor stability once injected (< 10 min [16]). To address this limitation, repeated injections of fresh microbubbles or continuous infusions can be administered to extend their circulation within the body, thereby enhancing the procedure's efficiency [17]. However, the half-life of microbubbles in the bloodstream is very short (in the order of 1–2 min) and the total dose of contrast agents administered to humans is limited. This means that microbubbles have to be reinjected very often (or infused) in very small quantities to maintain a constant concentration of agents over time. Reduced dose administration is detrimental to therapeutic efficacy [18]. Enhancing the stability of the sonosensitive agent would enable the use of smaller doses. Also, due to their size, conventional microbubbles cannot penetrate smaller vessels like capillaries. Using smaller agents, around a hundred nanometers, could enable greater extravasation by allowing access to these capillaries while preserving comparable opening in larger vessels [19,20].

Indeed, a compelling alternative to traditional microbubbles is the use of nanodroplets (NDs), composed of liquid phase perfluorocarbons encapsulated by a phospholipid shell [21]. Ultrasound can be used to vaporize these NDs, also known as phase-change contrast agents (PCCA), into microbubbles. Acoustic droplet vaporization (ADV) and the ensuing bubble cavitation under ultrasound exposure are able to induce BBB disruption and drug delivery [22]. For *in vivo* conditions at 37 °C, sufficient rarefaction pressure is required to vaporize the droplet's liquid core [23]. Apart from the core phase, the composition of NDs closely resembles that of bubbles [14,19,24]. Since the core of the droplet is in liquid state, with molecules packed more closely together, droplets are typically smaller than gaseous microbubbles [25], usually in the range of a hundred nanometers [26]. Stable droplets can be obtained by condensing commercial microbubbles [27]. The liquid core of NDs may result in a longer *in vivo* circulation time compared to microbubbles, preventing gas dissolution [26]. Despite this extended *in vivo* lifetime, this high stability requires the compensatory application of high acoustic pressure to vaporize the agent and transform it into a gas microbubble. The selection of the perfluorocarbon core is therefore decisive, as it will have a direct impact on the acoustic pressure required to vaporize it [14]. NDs containing liquid perfluorocarbon with boiling point above 20 °C has been employed to permeabilized the BBB with FUS [28,29] or through laser activation [30,31]. However, perfluorocarbons with low boiling points result in easier vaporization at lower acoustic pressures [23,25].

In this work, we used droplets containing octafluoropropane (C_3F_8, boiling point −37 °C) or decafluorobutane (C_4F_{10}, boiling point −2 °C). The droplets were obtained by a microbubble condensation process and are therefore smaller than the original microbubbles [27]. The NDs used is the present work were previously assessed for their ability to permeabilize the BBB in mice in 2013 and 2018 [22,32]. Chen et al. successfully delivered 3 kDa dextran to the mouse brain using C_3F_8 droplets without histological damages (600 kPa; f_0 = 1.5 MHz, 10,000 cycles of 6.7 ms, PRF = 5 Hz, exposure time = 5 min) [32]. Later, Wu et al. compared C_4F_{10} and C_3F_8 droplets for delivery of 40 kDa dextran to the brain. BBB opening in mice was successful for both droplets (f_0 = 1.5 MHz; 450 kPa for C_3F_8; 900 kPa for C_4F_{10}, 10,000 cycles of 6.7 ms; PRF = 5 Hz, exposure time = 5 min) though a subset of dark neurons were observed for the C_4F_{10} droplets BBB opening indicating potential adverse effects [22]. In both studies, ADV threshold experiments were conducted before the *in vivo* experiments, the FUS sequence was static, and the BBB opening was localized in the hippocampus [22,32].

With only these few studies published to date, the exploration of low-boiling perfluorocarbon NDs for BBB opening and drug delivery into the brain is still in its early stages and represents a promising field for further research. A precise understanding of the condensation process, along with the engineering of suitable FUS sequences for BBB opening for various applications, remains to be developed.

The first part of this study focused on understanding the microbubble condensation process and identifying the entities formed during this stage, using Transmission Electron Microscopy (TEM) and Cryo-TEM. To date, only one study reports Cryo-Transmission Electron Microscopy (Cryo-TEM) of low-boiling points perfluorocarbon NDs, and investigate the impact of storage at −80 °C on their morphology [33]. In this present work, cryo-TEM images with unprecedented resolution for droplets are presented, allowing to investigate the structure of lipids within condensed droplets. Recognizing the crucial need to understand the impact of ultrasound, particularly acoustic vaporization and cavitation, on ND suspensions [14], acoustic characterizations were carried out by analyzing the acoustic response and observing droplet vaporization using a microscope connected to a high-speed camera. FUS-induced BBB opening was conducted in mice. Adaptable protocols tailored to each application are proposed, creating a versatile toolbox for generating openings customized to specific needs (wide or localized) by adjusting ultrasound parameters and NDs. Finally, efficacy and safety were assessed using MRI, gross pathology and histology.

2. Material and methods

2.1. Material

1,2-distearoyl-sn-glycero-3-phosphocholine (DSPC) and 1,2-distearoyl-*sn*-glycero-3-phosphoethanolamine-N-[methoxy(polyethylene glycol)-2000] (DSPE-PEG2000) were purchased from Avanti Polar Lipids. C_4F_{10} and C_3F_8 were purchased from FluoroMed.

2.2. Nanodroplet formation

NDs were formed by condensation of microbubbles. As previously described [25,34], DSPC and DSPE-PEG2000 (molar ratio 9:1) were

dissolved in a phosphate bufferred saline (PBS)-based excipient solution (1×) containing 15 % (*v/v*) propylene glycol and 5 % (*v/v*) glycerol (PBS-15PG-5G) for a final lipid concentration of 1 mg/mL. 1.5 mL aliquots of the resulting lipid solution were packaged into 3 mL glass serum vials. The air in the vial headspace was exchanged with either C_3F_8 or C_4F_{10} perfluorocarbon gas. The microbubble emulsions were finally formed *via* standard agitation using a Vialmix shaker (Lantheus Medical Imaging).

As described in [35,36], microbubbles were then condensed into NDs by cooling microbubbles in an ethanol bath thermostated to −13 °C, followed by pressurization of the vial at 40 PSI with nitrogen gas (2800 mbar).

Size and concentration of the differents NDs were measured with a Nanosight LM10 (Malvern Panalytical) and an AccuSizer FX-Nano (Entegris). Nanosight measurements, using Nanoparticle Tracking Analysis (NTA), track individual particles in polydisperse suspensions. This method can measure suspensions within the particle size range of 10 nm to 1000 nm, with concentrations ranging from 1×10^7 to 5×10^9 particles/mL [37]. To ensure accurate measurements within the concentration range, ND suspensions were diluted in milli-Q water before each analysis (Camera Level: 16; Detection Threshold: 5; Temperature: 37 °C). Accusizer-based measurements rely on Single Particle Optical Sizing (SPOS), enabling the assessment of particle suspensions ranging in size from 150 nm to 10 µm [38]. Measurements were repeated three times using three different vials ($n = 9$) for C_3F_8 and C_4F_{10}.

2.3. Transmission Electron Microscopy (TEM)

The NDs were initially visualized through negative staining. Following the application of a glow discharge plasma to induce surface hydrophilicity, 3 µL of the suspension was placed on a 400-mesh carbon grid (Electron Microscopy Science). After 1-min, excess sample was removed using filter paper. Subsequently, a 2 % uranyl acetate solution (Laurylab) was applied to the grid's surface with the deposited sample for 30 to 50 s. Once again, excess liquid was absorbed using filter paper. The carbon grid was then examined using a JEOL 120 kV microscope (JEM 1400) equipped with a RIO 9 camera.

Cryogenic transmission electron microscopy (cryo-TEM) was also employed to observe the NDs. For this procedure, 3 µL of sample were applied onto freshly glow-discharged Quantifoil R2/2, 200 mesh grids, and then plunge-frozen into liquid ethane. Grids were observed in an electron microscope (Tecnai G20, FEG, FEI) operating at 200 kV, equipped with a K2 Summit direct-detection camera.

2.4. Acoustic characterizations

2.4.1. Acoustic Droplet Vaporization (ADV)

To characterize the acoustic droplet vaporization (ADV) threshold as function of the applied Peak negative Pressure (PNP), an optical microscope linked to a high-speed camera was used to observe the focal point of an ultrasound transducer, as detailed in [22] (Fig. 1-A). Briefly, the system featured an inverted microscope with a 60× immersion objective (Olympus IX71) connected to a high-speed camera (1000 fps, FastCam; Photron Inc.). A water-filled tank at 37 °C was attached to the microscope objective. A cuprophane tube (extremely thin cellulose membrane) with a diameter of 180 µm (Medicell Membranes Ltd) was positioned at the focal point of a focused transducer (active diameter 25 mm, focal depth 20 mm, focal spot length at −6 dB: 5 mm, focal spot width at −6 dB: 1 mm, Imasonic) with center frequency $f_0 = 1.5$ MHz and the microscope objective. The transducer, connected to a single-channel programmable generator (Image Guided Therapy), was accurately placed using a calibrated needle hydrophone (HNA-0400, Onda) at the focal length of the microscope objective. After hydrophone placement, the cuprophane tube was set at the focal length of the objective. A suspension of NDs (about 100 µL) was very gently injected (in 20 s) into the tube by hand, until the flow stabilized (after pushing

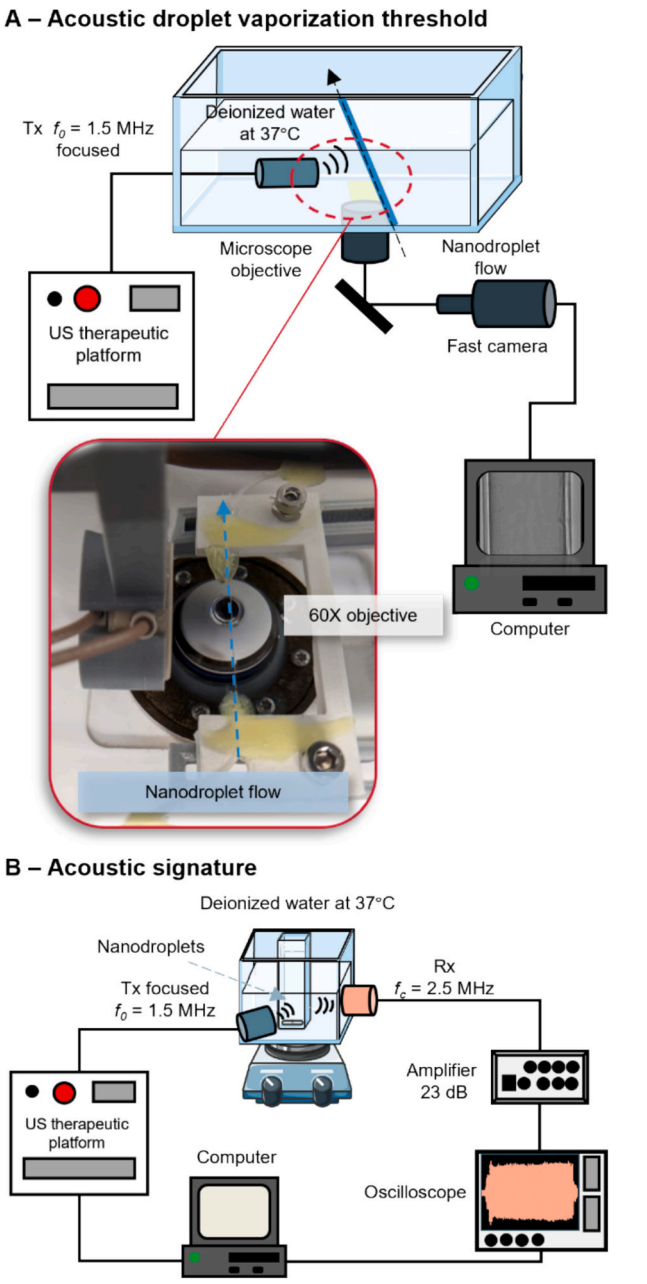

Fig. 1. Nanodroplet acoustic characterization: A - Detection of nanodroplet vaporization threshold using an inverted optical microscope and high-speed camera. B - Acoustic signature characterization device for nanodroplets.

was stopped) then a single ultrasonic pulse (pulse duration 50 cycles) was applied and the resulting vaporization events were video-recorded *via* a generator-synchronized camera. Recordings consisted of the 100 frames before the ultrasonic wave was triggered and 676 frames after triggering. For C_3F_8 NDs, videos were recorded for PNP ranging from 0 kPa to 1 MPa (nine measuring points), with a fresh ND bolus for each acquisition. For C_4F_{10} NDs, the signal was recorded for PNP ranging from 0 to 2.5 MPa (twelve measuring points). For a vial, each measurement was repeated at least three times (typically 5 to 7 times), and the entire experiment was replicated for three vials of C_3F_8 and three vials of C_4F_{10}. The droplets were diluted 2-fold in 0.9 % *w/v* NaCl before injection into the cuprophane tube.

2.4.2. Acoustic signature

Acoustic characterization was performed to measure freshly

vaporized microbubble harmonic and ultra-harmonic responses as a function of the PNP (Fig. 1-B). The NDs were diluted 10-fold with PBS-15PG-5G in a vial sealed in an atmosphere consisting of the same perfluorocarbon as that contained in the NDs. 100 μL of this dilution was injected into 40 mL of degassed milli-Q water and stirred in a custom-made chamber with mylar walls. Positioned centrally within a larger tank of degassed milli-Q water maintained at 37 °C, the NDs were stirred using a focused transducer (as described for ADV) with a center frequency $f_0 = 1.5$ MHz (PRF = 10 Hz; pulse duration 40 cycles) placed 20 mm from the chamber. Simultaneously, the acoustic response from droplet vaporization (to create gas-filled microbubbles) was captured with a 2.25 MHz ultrasonic focused transducer (active diameter 25 mm,

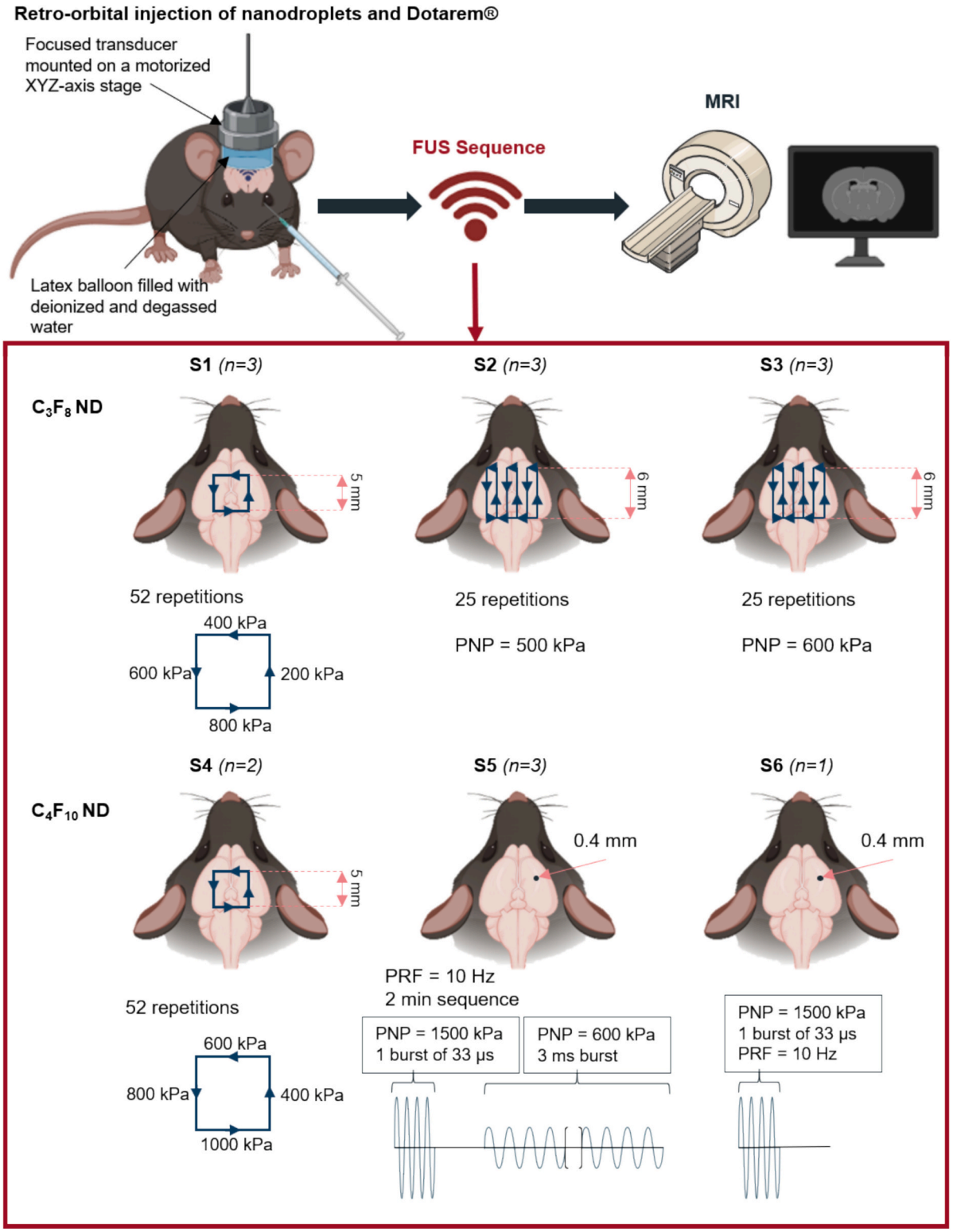

Fig. 2. BBB permeabilization with low-boiling point perfluorocarbon nanodroplets: schematic representation of the different stages and ultrasound sequences explored. In the "Results" section, the codes S1, S2, S3, S4, S5 and S6 have been employed to distinguish between ultrasound sequences used.

V304-SU, Olympus) positioned at 46 mm from the mylar chamber, perpendicular to the emission transducer. An ultrasound-absorbing material (Aptflex F48, Precision Acoustics Ltd) was placed on the opposite side to prevent multiple reflections.

The recorded signal was processed as described elsewhere [39]. Briefly, the signal observed on a digital oscilloscope (MSO Series 5 Tektronix), at a sampling frequency of 1.6 GHz, was transferred to a computer for data analysis (Matlab Release 2018b, The MathWorks). The area under the curve (AUC) of the second harmonic (3.000 MHz ± 0.030 MHz), the first ultraharmonic (2.250 MHz ± 0.020 MHz), indicative of the nonlinear response induced by agent vaporization and the broadband noise (2.625 MHz ± 0.225 MHz) were calculated. AUC ratios (AUCR) between the microbubble signal and the signal from the mylar chamber filled with water only were also computed. For ND C_3F_8, the signal was recorded for PNP ranging from 200 kPa to 1.5 MPa (10 measurements). For C_4F_{10} NDs, the signal was recorded for PNP ranging from 500 kPa to 2.5 MPa (10 measurements). Each measurement was repeated three times, with a bolus of fresh NDs for each acquisition, and the entire experiment is replicated for three vials of each ND type. The appearance of the 2 f_0 peak was considered a marker of microbubble formation, while the appearance of the 1.5 f_0 peak served as a marker of the microbubble destabilization threshold [12]. Furthermore, broadband noise was a characteristic of inertial cavitation.

2.5. FUS-induced BBB opening

2.5.1. FUS sequences

BBB opening experiments with C_3F_8 and C_4F_{10} NDs were carried out on female C57BL/6 mice (21.0 ± 3.1 g). Animals were anesthetized with 1.5 % isoflurane in an O_2/air mixture (50/50, *v/v*). Compared to O_2 alone, mixing O_2 with medical air to carry gas anesthesia extends the circulation time of sonosensitive agents *in vivo* [40]. A bolus containing 100 μL of Dotarem® (Gd-DOTA, Guerbet) and 50 μL of undiluted ND suspension was injected intravenously *via* the retro-orbital cavity. All animal experiments were carried out in accordance with the recommendations of the European Community (2010/63/EU) and French national committees (law 2013–118) for the care and use of laboratory animals. The experimental protocol was approved by a local ethics committee for animal experimentation (Ile-de-France n°044) and by the French Ministry of Agriculture (APAFIS #34522–2,022,010,412,087,915 v1).

Focused ultrasound was delivered using the same system as in Hugon et al. [41]. Briefly, a spherically focused transducer (active diameter 25 mm, focal depth 20 mm, focal spot length at −6 dB: 5 mm, focal spot width at −6 dB: 1 mm, Imasonic) centered at 1.5 MHz was linked to a single-channel programmable generator (Image Guided Therapy), mounted on a motorized XYZ-axis stage, and positioned above the mouse head maintained under anesthesia (Fig. 2). To couple the device to the mouse head, a latex balloon filled with deionized degassed water and coupling gel was used. The distance between the transducer and the skull was adjusted to precisely target the center of the brain at the focal distance. Multiple ultrasonic sequences were explored, as described in Fig. 2. Table 1 provides a summary of the ultrasound parameters employed across the different *in vivo* and *in vitro* sequences.

For ND C_3F_8, three ultrasonic sequences were explored. The first sequence (labeled S1 in Fig. 2) outlined a 5 mm square by transmitting ultrasound quasi-continuously (91 % duty cycle). The emission stopped with each change in motor direction (moving at 10 mm/s), and different PNP were transmitted to each side of the square. This square pattern was repeated 52 times, resulting in a total sequence time of 121 s. The transducer transmitted *in situ* PNP along the sides of the square at 200 kPa, 400 kPa, 600 kPa, and 800 kPa. This experiment was repeated identically on three separate animals. The second and third sequences (labeled S2 and S3 in Fig. 2) aimed to permeabilize the entire brain through a continuous XY raster scan (6 mm × 6 mm, 1.2 mm step, 10 mm/s). The scan was repeated 25 times, resulting in a total sequence time of 127 s. The PNP transmitted *in situ* was 500 kPa for sequence S2, and 600 kPa for S3 sequence (69 % duty cycle). These sequences (S2 and S3) were repeated identically on three separate animals. A sham sequence was also performed after C_3F_8 ND injection for one animal.

Table 1
Ultrasound parameters used for *in vitro* and *in vivo* experiments.

In vitro experiments (f_0 = 1.5 MHz)

Acoustic droplet vaporization threshold

PNP	n° of cycles	PRF
0, 0.2, 0.25, 0.3, 0.4, 0.5, 0.7, 0.75, 1 MPa for C_3F_8 NDs 0, 0.3, 0.5, 0.7, 0.8, 0.9, 1, 1.2, 1.5, 1.7, 2, 2.5 MPa for C_4F_{10} NDs	50	1 pulse

Acoustic signature

PNP	n° of cycles	PRF
0.2, 0.3, 0.4, 0.5, 0.6, 0.7, 0.8, 1, 1.2, 1.5 MPa for C_3F_8 NDs 0.5, 0.8, 0.9, 1, 1.1, 1.2, 1.5, 1.7, 2, 2.5 MPa for C_4F_{10} NDs	50	10 Hz

In vivo experiments (f_0 = 1.5 MHz)

Sequence #	Tranducer trajectory shape	PNP	Duty cycle	Effective duty cycle	Total duration / burst info
S1	Mechanical scan Square outline	0.2, 0.4, 0.6, 0.8 MPa	91 %	4.3 %	121 s
S2	Mechanical scan Filled square	0.5 MPa	69 %	2 %	127 s
S3	Mechanical scan Filled square	0.6 MPa	69 %	2 %	127 s
S4	Mechanical scan Square outline	0.4, 0.6, 0.8, 1 MPa	91 %	4.3 %	121 s
S5	Single spot - not moving	1 burst of 33 μs (50 cycles) at 1.5 MPa followed by 3 ms burst at 0.6 MPa. PRF = 10 Hz. Duration = 2 min.			
S6	Single spot	1 burst of 33 μs (50 cycles) at 1.5 MPa. PRF = 10 Hz			

For C_4F_{10} ND, three sequences were explored. The first sequence (labeled S4 in Fig. 2) mirrored the C_3F_8 ND S1 sequence, outlining a 5 mm square and transmitting quasi-continuous ultrasound. The *in-situ* PNP transmitted along the sides of the square were 400 kPa, 600 kPa, 800 kPa, and 1000 kPa. This experiment was repeated identically on two separate animals. Only two animals were used (and not three, as for the others experiments) given the expectation that C_4F_{10} requires a higher acoustic pressure for activation than C_3F_8 [42]. This experiment was repeated identically on two separate animals. The second C_4F_{10} ND sequence (labeled S5 in Fig. 2) focused at single point and transmitted an initial ultrasonic burst at 1500 kPa PNP (1 pulse of 33 μs followed by a 77 μs pause) to vaporize the droplets. This was followed by a 600 kPa PNP sequence (3 ms pulse) to oscillate the freshly vaporized bubbles and permeabilize BBB. The sequence was repeated at a PRF = 10 Hz, *i.e.,* a duty cycle of 3 % for 2 min. The purpose of this sequence was to vaporize C_4F_{10} droplets while minimizing the duration of the vaporization pressure (33 μs) to avoid tissue damage. Indeed, conventional microbubbles showed adverse effects in rodent brains when pressures exceeding 1000 kPa were applied [43]. The quasi-continuous emission of this high acoustic pressure was, therefore, risky for the animal, making it difficult to open the BBB as widely as motorized trajectories. We, therefore, chose to restrict the opening zone for these first high-amplitude trials. The experiment was repeated identically on three separate animals. Finally, a third sequence (labeled S6 in Fig. 2) involved sending only an ultrasonic burst at a PNP of 1500 kPa (1 pulse of 33 μs, PRF = 10 Hz) vaporize

the droplet and evaluate if ADV alone was sufficient to permeabilize the BBB. This experiment was conducted on a single animal.

For all the experiments described above, the stated PNP takes into account the passage of the skull, assuming a transmission factor through the skull of 80 % at 1.5 MHz for a C57/Bl6 mouse of 21 g [44].

2.5.2. Magnetic Resonance Imaging

Immediately after the FUS sequence, the animal was placed under MRI. Contrast-enhanced T_1-weighted MRI were acquired with a 7 T/90 mm MRI scanner (Pharmascan scanner,) using an MSME sequence (TE/TR = 5/300 ms, matrix = 256 × 256 × 64, 12 averages, acquisition time = 8 min). For the S2, S3 and S5 sequence, T_2-weighted images were acquired using a RARE sequence (TE/TR = 5.6/3000 ms, RARE factor = 8, matrix = 256 × 256 × 64) 48 h after opening of the BBB to verify the absence of damage induced by the application of high acoustic pressures.

2.5.3. Histological analysis

Animals receiving S2 and S3 sequences were sacrificed after T_2-weighted MRI scans (2 days after FUS). Intracardiac perfusion was performed with 0.9 % NaCl delivered at a flow rate of 8 mL/min. The brain was then removed and immersed in an isopentane bath at −30 °C for 10 min. The isopentane was then removed and the brain was placed in a freezer at −80 °C before being cut. The frozen brains were sectioned transaxially through the striatum at a thickness of 14 μm using a cryostat (Leica CM3050 S, Leica Biosystems). The sections were then mounted on SuperFrost Ultra Plus™ slides (FisherScientific) and stored at −80 °C until further histological analyses, with hematoxylin-eosin staining. Slides with frozen brain sections were fixed in 10 % neutral buffered formalin for 30 min and then washed with distilled water. Standard hematoxylin and eosin (H&E) staining was performed using Harris hematoxylin and Eosin Y alcoholic (Sigma-Aldrich). Transmitted light images of the stained tumor sections were acquired using an Axio Observer 5 microscope (Zeiss) at 20× magnification. Image post-processing was conducted with ZEN software (v2.6, Zeiss).

3. Results and discussion

3.1. Physicochemical characterization of nanodroplets

3.1.1. Size and concentration measurements

The suspensions of NDs originate from polydisperse microbubbles and, therefore, are inherently polydisperse themselves. The average size and concentration of NDs are presented in Table 2. All data for a given perfluorocarbon have been gathered to compute the first and ninth deciles, the median, and span ($(d_{90}-d_{10})/d_{50}$) of the size distribution (Table 2), and, to generate the cumulative frequency graph measured with Nanosight and AccuSizer (supplementary fig. 1).

Discrepancies arised in the results obtained based on whether the measurement was conducted using NTA (Nanosight) or SPOS (AccuSizer). NTA measurements yielded higher concentration values and a smaller mean size compared to those obtained with SPOS. Specifically, concentrations measured using NTA were $(2.6 \pm 2.9) \times 10^{13}$ particles/mL and $(4.8 \pm 4.1) \times 10^{12}$ particles/mL for C_3F_8 NDs and C_4F_{10} NDs, respectively. SPOS concentration measurments were $(8.2 \pm 4.2) \times 10^{9}$ particle/mL for C_3F_8 NDs and $(9.7 \pm 4.3) \times 10^{9}$ particle/mL for C_4F_{10} NDs. Given the same measuring device, the average sizes were similar regardless of the type of perfluorocarbon evaluated. Mean diameters measured using NTA were 140 ± 14 nm and 160 ± 17 nm for ND C_3F_8 and C_4F_{10} ND, respectively. Mean diameters measured using SPOS were 317 ± 6 nm for C_3F_8 ND and 317 ± 15 nm for C_4F_{10} ND. Identical NDs to those in this study have been characterized using Nanoparticle Tracking Analysis (mean diameter = 171 ± 3 nm; concentration = 2.8×10^{11} particles/mL for C_3F_8; mean diameter = 183 ± 3 nm; concentration = 1.3×10^{11} particles/mL for C_4F_{10}) [22]. The same NDs have also been measured using single-particle optical sizing (mean diameter = 320 nm; concentration = 9.89×10^{9} particles/mL for C_3F_8; mean diameter = 340 nm; concentration = 1.25×10^{10} particles/mL for C_4F_{10}) [45]. C_3F_8 NDs with a phospholipid shell obtained through a condensation process were also measured using Nanoparticle Tracking Analysis (mean diameter = 221 ± 3 nm; concentration = 9.7×10^{10} particles/mL) and dynamic light scattering (mean diameter = 206 ± 6 nm) [46].

Our findings regarding the characterization of NDs size and concentration highlight the challenge of identifying a reliable and robust method for this purpose. Specifically, the concentrations measured using SPOS are three orders of magnitude lower than NTA measurments. The higher concentration measured by the Nanosight compared to the AccuSizer might be attributed to the fact that the detection limit of the AccuSizer is above 150 nm, which corresponds to the predominant size measured with the Nanosight.

3.1.2. Transmission electron microscopy: What lies within a vial of nanodroplets produced through condensation?

Fig. 3 shows different TEM images of negatively stained samples and Fig. 4 shows cryo-TEM images. In negative staining, the contrast relied on the interaction between the sample and the used dye, in this case uranyl acetate. In cryo-TEM the frozen sample was directly observed, and the contrast was determined by the electron density of the sample: the higher the electron density, the darker the observed image. In the negative staining experiment, a suspension of microbubbles containing C_4F_{10} was examined. The bubbles were easily distinguishable, forming a foam-like coalesced structure on the grid with a bright core and a very thin dark wall, as illustrated in Fig. 3 (an example marked as A). The ND suspensions (C_3F_8 and C_4F_{10}) were also observed in negative staining, and similar characteristics can be identified for these two samples: relatively clear circular shapes with a double contour that tended to appear in the foreground (labeled as B once in each image in Fig. 3) and a background of slightly less contrasting circular shapes (labeled as C once in each image in Fig. 3). The entities labeled as objects (B) were likely droplets. Concerning the array of circular entities in the images background (objects C), the most plausible assumption is that they corresponded to liposomes (devoid of perfluorocarbon). Cryo-TEM images of liposomes with a composition very similar to ours have been reported in the literature [47] and depict similar object as objects C. Moreover, Owen et al. used negative staining TEM to visualize phospholipid microbubbles, and their observation is similar to the one depicted in Fig. 3 [48].

CryoTEM images of NDs suspensions revealed distinct object types identified as A, B, and D in Fig. 4 (labeled only once in each photo). Objects A manifested as nearly white circular shapes with a black outline. Objects B consisted of darker shapes entwined with small rods approximately 3 nm thick (highlighted by a white arrow in Fig. 4).

Table 2
Size distribution and concentration C_3F_8 and C_4F_{10} nanodroplets measured by Nanosight (NTA) and AccuSizer (SPOS). $n = 3$ vials; SD: standard deviation among vials. The averaged values of d_{10} (first decile), d_{50} (median), d_{90} (ninth decile), and span are based on measurements from the 3 vials.

	Device	Mean ± SD (nm)	d_{10} (nm)	d_{50} (nm)	d_{90} (nm)	span	concentration ± SD (particles/mL)
C_4F_{10} ND	NanoSight	160 ± 17	103	139	248	1.0	$(4.8 \pm 4.1) \times 10^{12}$
	AccuSizer	317 ± 15	270	293	380	0.4	$(9.7 \pm 4.3) \times 10^{9}$
C_3F_8 ND	Nanosight	140 ± 14	95	120	218	1.0	$(2.6 \pm 2.9) \times 10^{13}$
	AccuSizer	317 ± 6	270	280	360	0.3	$(8.2 \pm 4.2) \times 10^{9}$

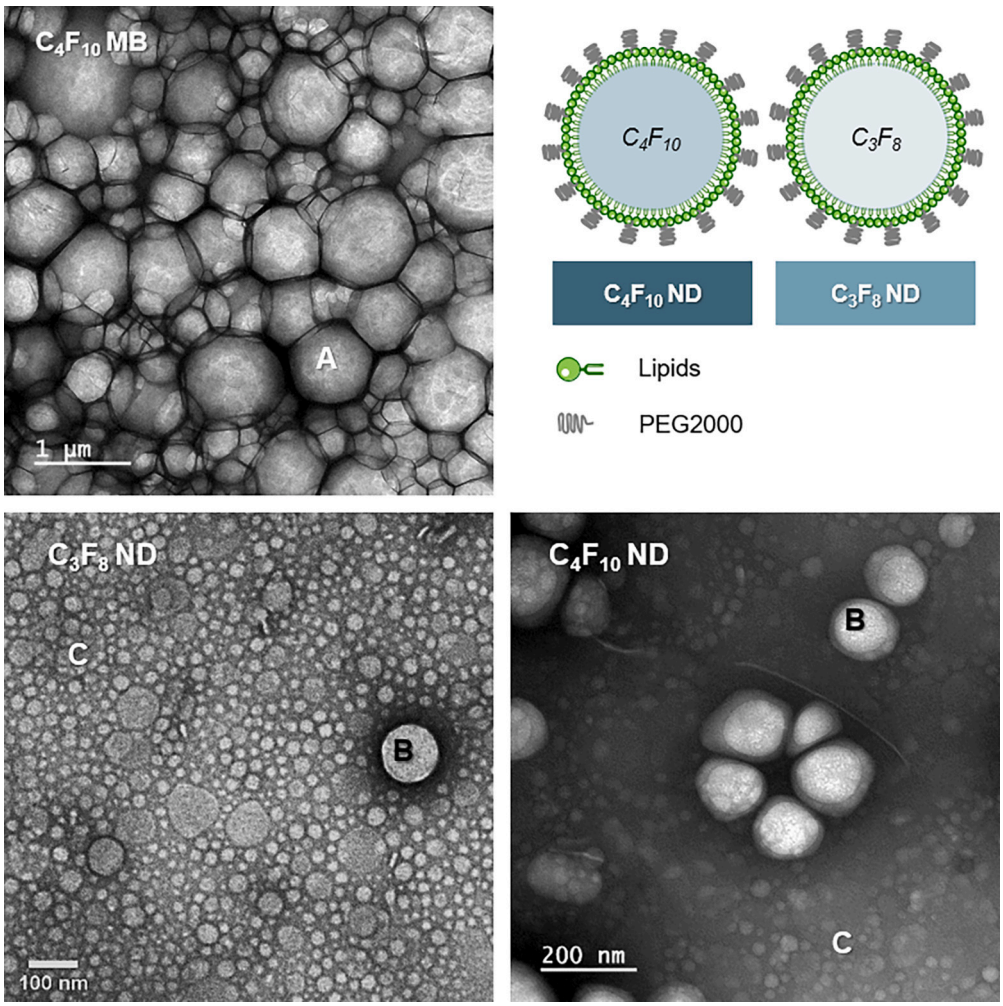

Fig. 3. Negative-stained TEM images of microbubble and nanodroplet suspensions. Three types of objects identified: A, B and C. A: microbubble; B: nanodroplet, C: liposome. Up-right: Illustration of the different nanodroplets studied.

Objects D represented a superposition of both A and B. During CryoTEM imaging of NDs, the D objects were observed to undergo movement under the electron beam of the microscope: the light circular shape expanded under the electron beam, adhering to the contour of the dark circular shape (see supplementary material). Similar objects A, B, and D were observed in droplets suspensions containing both C_4F_{10} and C_3F_8, but in smaller quantities for the C_3F_8 samples. To gain a deeper understanding of the observed phenomena, we conducted a control experiment: a phospholipid suspension was "condensed" without undergoing the microbubble activation step; the vial lacked perfluorocarbon and agitation. The cryoTEM images of the pressurized liposome suspension revealed several comparable circular shapes with varying degrees of contrast (identified as C for one of them in Fig. 4) and small rods (indicated with a white arrow for one of them in Fig. 4). C structures were found in all suspensions imaged by cryo-TEM but not shown in each image of Fig. 4.

Within our droplet suspensions, the most electron-dense component was perfluorocarbon, as it was rich in fluorine atoms. Our working hypothesis was that objects labeled as A represent bubbles, and objects labeled as B correspond to droplets. Consequently, the lighter structure within a darker shape (objects D) may indicate a droplet undergoing vaporization due to the electron beam of the microscope. Another hypothesis suggests that the entangled rods within the droplets (indicated by white arrows in Fig. 4) correspond to lipids that have left the interface upon pressurization during condensation and are currently in suspension in the liquid perfluorocarbon. This latter hypothesis aligns with images of pressurized liposomes, where alongside circular shapes resembling liposomes (objects C), there are also similarly sized rods (highlighted with white arrows). Until recently, TEM images of C_3F_8 or C_4F_{10} liquid perfluorocarbon NDs were notably absent from the scientific literature. A recent publication by a team at Sunnybrook Research Institute (Toronto, Canada) filled this gap, presenting cryoTEM images of C_4F_{10} phospholipid NDs [33]. Their droplets were generated by sonication of Definity lipid solution (0.75 mg/mL, Lantheus Medical Imaging) and pentobarbital (25 µg/mL). The solution was then placed in a C_4F_{10} atmosphere, and bubbles were formed through VialMix agitation, followed by ND condensation as described in the present paper. They investigated the influence of storage at −80 °C (ranging from 0 to 14 days) on their droplets [33]. Their findings revealed a shell and a denser core of liquid perfluorocarbon, with a noticeable loss of circularity as storage time at −80 °C increased [33]. In our case, the observed droplets were stored at −80 °C for 8 to 10 days before examination. Their images exhibited structures identical to ours (Fig. 4). The non-circular shape of our droplets may be attributed to potential artifacts arising from freezing the preparation and then subjecting them to high vacuum. While this recent article stands as the only one, to our knowledge, showcasing perfluorocarbon NDs at low-boiling temperatures imaged by cryo-TEM, we can leverage insights from several studies to analyze our images. Javadi et al. introduced "eLiposomes" designed for ultrasound drug delivery, made up of liposomes encapsulating perfluorohexane emulsions (C_6F_{14}) [49]. The resulting eLiposomes were examined through negative staining and cryo-TEM, revealing clear

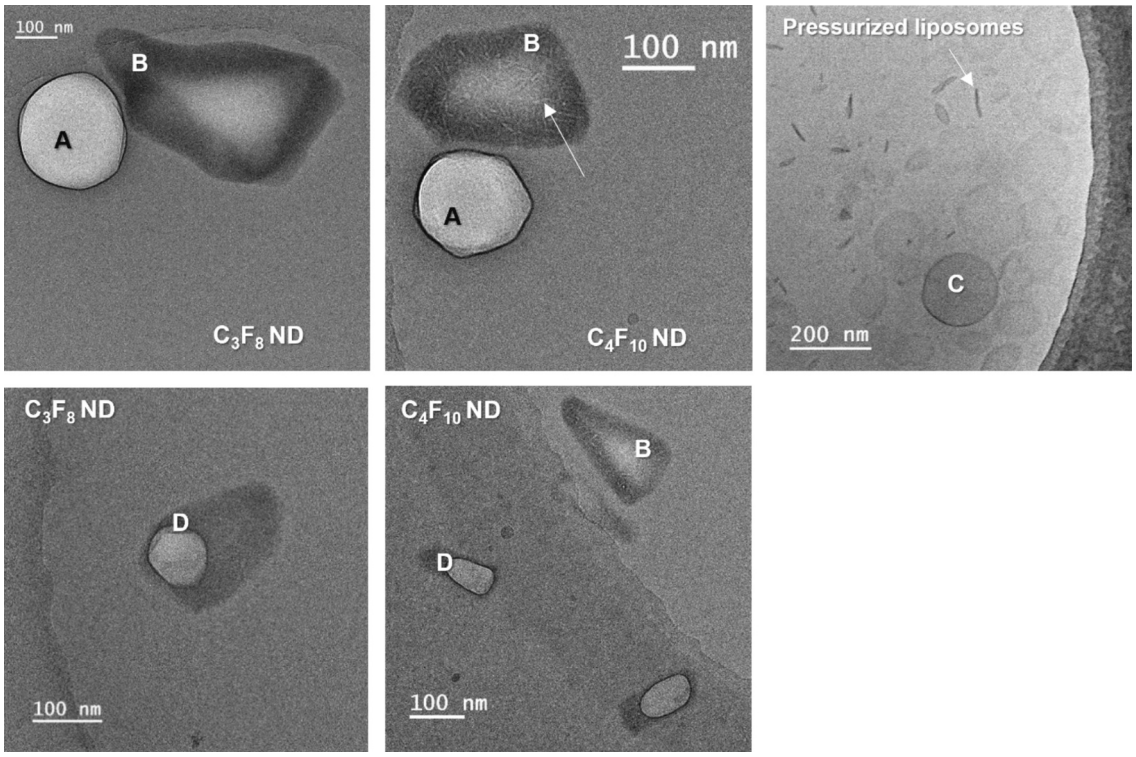

Fig. 4. Cryo-TEM images of nanodroplet and liposome suspension under pressure. Five object types identified: A, B, C, D, and objects arrowed in white. Each object type is identified only once per image in which it is found. A: bubble; B: nanodroplet; C: liposome; D: vaporizing droplet; arrows: lipids retracted on themselves with the overpressure linked to the condensation process.

spheres ranging between 100 and 200 nm within larger, darker, non-spherical structures. The sphere sizes align with the DLS measurements of the emulsion reported in the publication, leading the authors to conclude that these are C_6F_{14} emulsions encapsulated within a DMPC liposome structure [49]. These images share similarities with the cryo-TEM observations of our ND suspensions, where a clear sphere is observed on a darker object (object B in Fig. 4). However, our conclusions differ as we hypothesize that the light-colored objects we observe in Fig. 4 do not contain liquid perfluorocarbon due to its high electron density. Lastly, Hernandez et al. conducted a study presenting cryo-TEM images of C_3F_8 phospholipidic nanobubbles [50]. The images depicted spherical shapes with a delineated contour and a darker, diffuse center. In this publication, the darker central part is identified as C_3F_8 gas. Furthermore, they produced films showcasing C_3F_8 escaping from the bubble's shell under the electron beam of the microscope, illustrating a visible decrease in the density of the nucleus under the electron beam (doi: https://doi.org/10.1038/s41598-017-13,741-1, *Supplemental Movies S1–S3)* [50]. The white spheres with a black outline observed in cryo-TEM (objects A in Fig. 4) may potentially be air bubbles from which the perfluorocarbon has "escaped" and localized around its contour.

3.1.3. Liposomes within nanodroplets suspensions

TEM images emphasized some limitations regarding Nanosight measurement. Indeed, by contextualizing TEM images alongside Nanosight measurements, we can critically evaluate the objects measured by the latter device. Besides, a microbubble suspension comprises a mixture of gas-filled bubbles and water-filled liposomes of approximately a hundred nanometers in size [51,52]. Therefore, it can be inferred that a nanodroplet suspension resulting from microbubble condensation contains a blend of droplets and liposomes, as observed in our TEM images. Consequently, distinguishing between these populations during measurement can pose challenges. Therefore, we can hypothesize that the concentration measured by Nanosight includes both liposomes and nanodroplets. Additionally, the TEM images show that liposomes are generally smaller than nanodroplets. Consequently, we can also assume that the presence of liposomes lowers the average size measured by Nanosight.

In fact, Woodward et al. proposed a method to make nanodroplets containing low boiling point perfluorocarbon without liposome in the final solution by using a probe sonicator [53]. They argue that a significant drawback of the microbubble condensation method is the presence of a substantial number of coexisting liposomes in the solution, which can result in suboptimal stability [53]. By employing low power sonication in a lipid solution containing liquid C_4F_{10} at −10 °C, they report an encapsulation efficiency of liquid C_4F_{10} in phosopholipidic droplet exceeding 99 % [53].

Batchelor et al. proposed a method to discriminate nanobubbles when acquiring NTA measurements with a Nanosight NS300 [51]. By using a camera level between 3 and 5, they suggest that only nanobubbles will be detected due to their higher relative scattering [51]. In the present study measurements were conducted with a camera level of 16 and a detection threshold of 5 on a Nanosight LM10, not an NS300 Model. Differentiating between droplets and liposomes, however, is more challenging than distinguishing between bubbles and liposomes.

3.1.4. Conclusion on physicochemical characterizations

During condensation of microbubbles, due to shell shrinking, it is very likely that nanodroplets coexist with liposomes and some bubbles. This emphasizes the need for caution when interpreting methods for measuring concentration and suspension size, as these methods do not differentiate between these different elements. Moreover, unlike what one would expect, lipids appear to be suspended in the perfluorocarbon nanodroplets, probably from the pressurization/condensation process.

3.2. In vitro acoustic characterization

The acoustic behavior of ND suspensions was then characterized *in vitro*. Fig. 5 shows the observed vaporization events at 37 °C on the inverted microscope as a function of the PNP applied. The percentage of observed vaporizations was calculated based on all videos captured at a specific pressure ($n = 5$ or more). In practical terms, for a given pressure and 5 videos, if one or more vaporization events were observed in 4 of those videos, the resulting percentage was 80 %. Unfortunately, exact counting of the number of vaporization events is challenging, as the newly vaporized bubbles appear in several imaging planes of varying clarity and proximity, complicating image processing. The vaporization probability was then averaged over the 3 vials of the same formulation that were tested. 80 % of the observed vaporization probability was considered as the threshold for a given type of ND [54]. At 37 °C, C_3F_8 droplets vaporized at pressures of 300 kPa and above. It should be noted that rare cases of spontaneous vaporization of C_3F_8 ND (PNP =0 kPa) have been observed. For C_4F_{10} droplets, vaporization occurred at higher pressures, specifically at 1.15 MPa.

The outcomes of acoustic signal measurements at 37 °C are presented in Fig. 6, illustrating a reprensentative graph of Fast Fourier transform for C_3F_8 ND and C_4F_{10} ND along with the 2 f_0, 1.5 f_0 and broadband AUCR as a function of the applied PNP graphs. Using our experimental setup, the appearance of the 2 f_0 and 1.5 f_0 peaks in the Fast Fourier transform plot corresponded to a 5 dB AUCR, while the appearance of broadband noise between these two peaks corresponded to 2 dB, thus establishing 5 dB as the threshold for peak appearance and 2 dB as the threshold for broadband noise on the presented graph.

The 2 f_0 AUCR quantification served as a quantification of microbubble cavitation intensity, confirming their presence in the ultrasound-exposed suspension. As the applied pressure increased, so did the extent of cavitation. Notably, cavitation in droplets containing C_4F_{10} (AUCR exceeding 5 dB between 650 kPa and 1.1 MPa) occurred slightly earlier than the vaporization threshold observed in the activation experiment under the inverted microscope (exceeding 1.1 MPa). However, some vaporization events were observable at pressures as low as 650 kPa on the inverted microscope device, accounting for approximately 10 % (Fig. 5). The cavitation threshold for C_3F_8 ND was calculated to occur between 450 and 500 kPa.

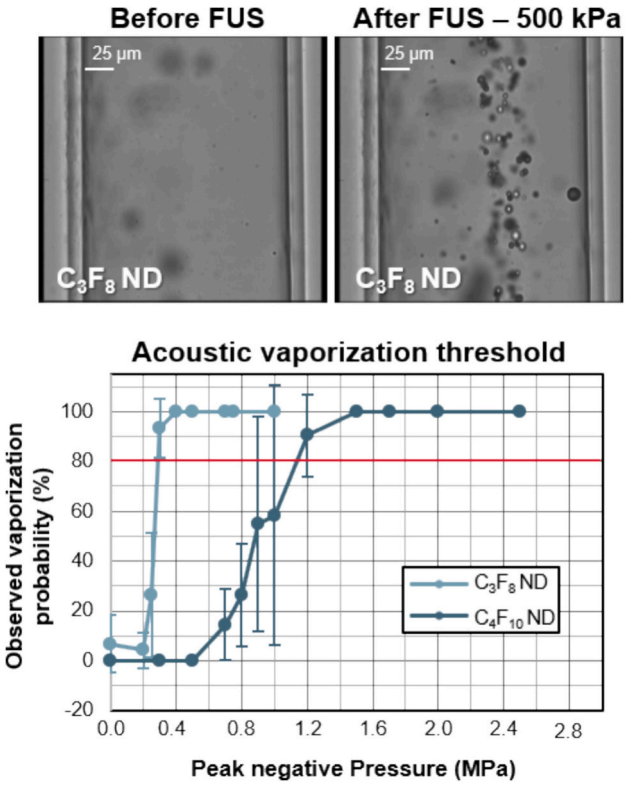

Fig. 5. Acoustic Droplet Vaporization visualized through optical microscopy with a high-speed camera. Example images captured before and after FUS emission for C_3F_8 ND suspension (top). Vaporizations observed across different suspensions as a function of PNP (bottom): each point represents the average vaporization probability at the corresponding pressure for all tested vials of the same formulation.

The AUCR of the 1.5 f_0 ultraharmonic represents the microbubble destabilization threshold. Once more, as the applied pressure increased, the extent of cavitation also increased. Notably, the thresholds for the appearance of the second harmonic and the 1.5 f_0 ultraharmonic were closely aligned. Thus, the destabilization threshold happened between 450 and 500 kPa for C_3F_8 ND and between 0.9 and 1.2 MPa for C_4F_{10} ND.

Finally, the AUCR between harmonics and ultraharmonics was broadband noise and represented inertial cavitation. Here, broadband noise between the 1.5 f_0 ultraharmonic and the second harmonic components was characterized. In a foreseeable way, inertial cavitation tended to occur when the applied pressure was high. Broadband noise was detected at PNP starting between 550 and 600 kPa for C_3F_8 ND and between 0.95 and 1.15 MPa for C_4F_{10} ND.

The different observed thresholds, as a function of the applied PNP or Mechanical Index (MI) for the different acoustic characterizations, are compiled in Fig. 7. MI enables comparison across multiple experiments conducted at different center frequencies, while other parameters remain constant [55]. The 80 % vaporization probability threshold represented a singular pressure point, denoted where the curve in Fig. 5 intersects the 80 % threshold. The detection thresholds of 2 f_0, 1.5 f_0 and broadband noise form a range, as they encompass the three observations from the three measured flasks without averaging.

In vitro acoustic characterization of NDs is crucial for the preclinical development of these agents, specifically to determine their vaporization threshold and cavitation regime, ensuring their potential *in vivo* use without causing tissue damage.

It is noteworthy that in droplet form (prior to vaporization), the signal is weak, as the agent is only slightly compressible and does not reflect ultrasound. As depicted in Fig. 7, it becomes obvious that for C_4F_{10}, the detection thresholds for harmonics and ultraharmonics are at pressures lower than the observed vaporization threshold pressure with the high-speed camera on the inverted optical microscope. This observation might be attributed to the limited number of droplets captured within the optical field during the experiment, potentially underestimating the vaporization threshold if vaporization occurs outside the field of view. Additionally, the two measurement devices differ: droplets are either suspended in water or flowing diluted in saline. Consequently, the droplets experience different surrounding pressures, which can influence the vaporization threshold [54]. The vaporization and cavitation pressures for NDs containing C_3F_8 are within a safe pressure range for potential *in vivo* use. However, the vaporization pressure for C_4F_{10} poses a higher risk for *in vivo* application at the tested frequency. Nevertheless, given the cavitation thresholds below 1 MPa, there is potential for promising *in vivo* trials.

Several factors influence the vaporization threshold of droplets, with key parameters including the choice of perfluorocarbon (boiling temperature), droplet size, experiment temperature, and applied acoustic parameters. As highlighted in the literature review by Lea-Banks et al., bigger droplets are easier to vaporize [26]. Conversely, in experiments where NDs resulting from the condensation of C_3F_8 and C_4F_{10} microbubbles or a mixture of the two perfluorocarbons with a phospholipidic shell were acoustically vaporized ($f_0 = 8$ MHz, MI = 0.04) at different temperatures [42], the probability of vaporization is temperature-dependent. Herein, at 34 °C, under the specified ultrasonic parameters, there is a 50 % chance that NDs containing C_3F_8 will vaporize [42]. In contrast, achieving similar chances of NDs containing C_4F_{10} vaporizing under the same conditions requires heating to 69 °C [42].

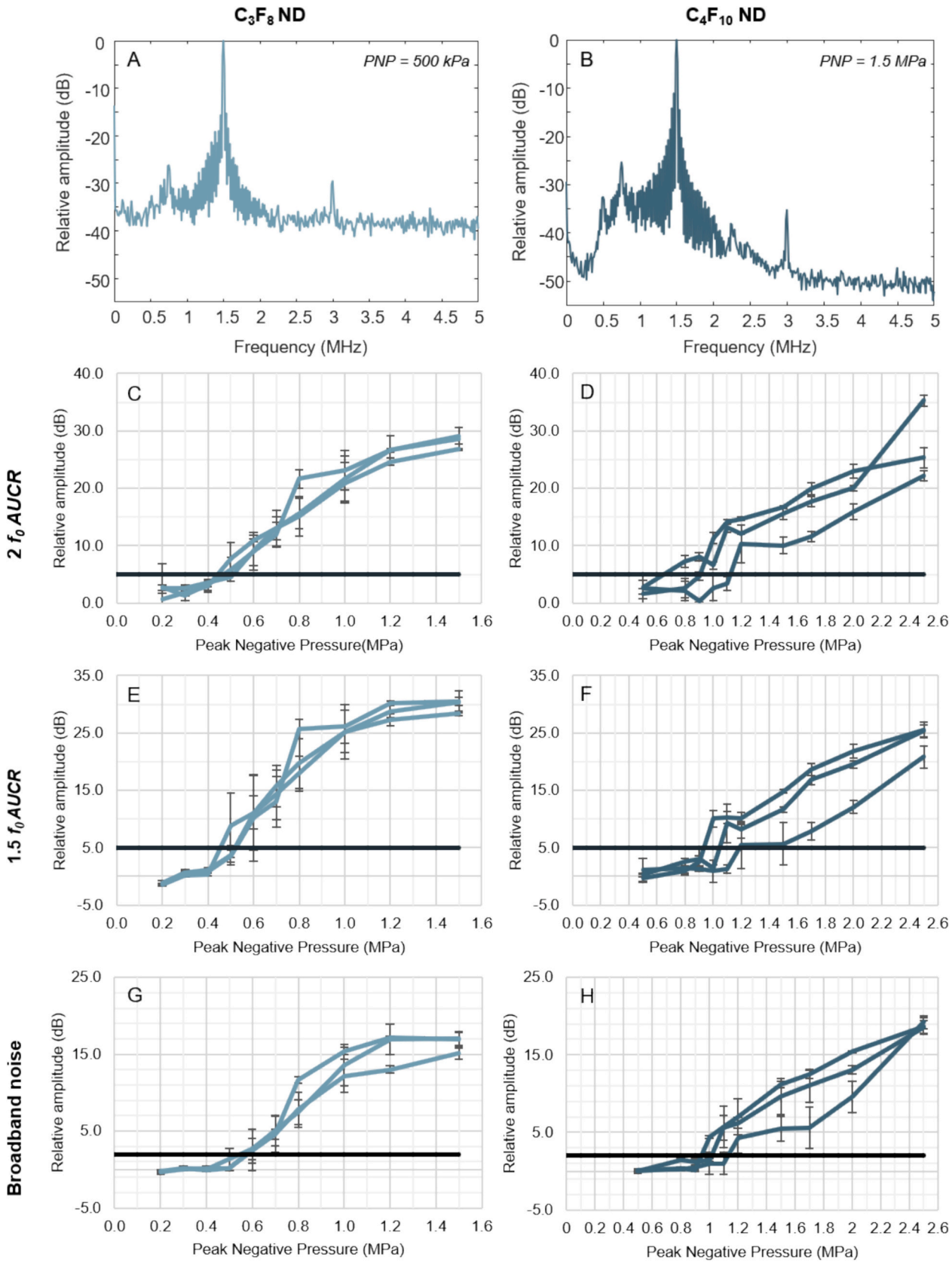

Fig. 6. Acoustic response of vaporized nanodroplets. A, B: Fast Fourier transform plot at an applied PNP of 500 kPa (C_3F_8 ND) and 1.5 MPa (C_4F_{10} ND). C, D: AUCR of the second harmonic plotted as a function of the applied PNP. E, F: AUCR of the ultraharmonic 1.5 f_0 plotted as a function of the applied PNP. G, H: AUCR of the broadband signal between 1.5 f_0 and 2 f_0 plotted as a function of the applied PNP. C to H: One point corresponded to a measurement repeated 3 times. For each type of perfluorocarbon, the experiment was reproduced for 3 different vials.

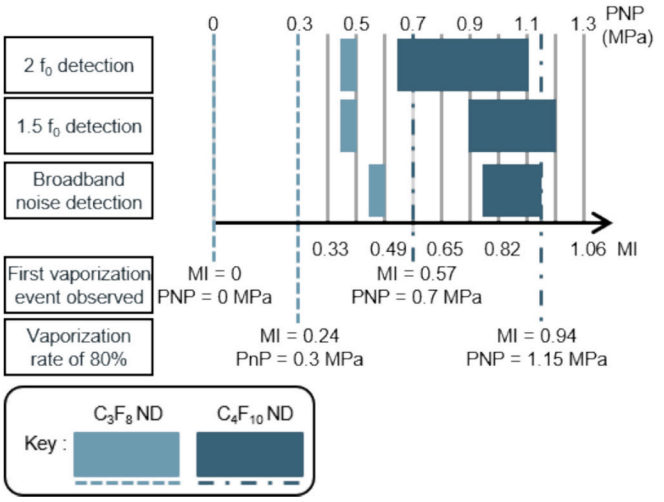

Fig. 7. All thresholds observed in *in vitro* acoustic characterization as a function of applied PNP and mechanical index (MI) for a central frequency of 1.5 MHz.

Li et al. conducted a study on the vaporization thresholds of phospholipidic droplets containing various perfluorocarbons: C_3F_8, C_4F_{10}, C_5F_{12}, and C_6F_{14}, with boiling points of −37 °C, −2 °C, 28 °C, and 60 °C, respectively [56]. To assess the cavitation threshold, the droplets were diluted in degassed water within a plastic cuvette at 37 °C. The suspension was excited with an ultrasonic wave of a center frequency of 1.24 MHz (15 cycles, PRF = 20 Hz), and the signal was received by an unfocused transducer with a center frequency of 40 MHz. The results showed a 50 % cavitation probability at 6.86, 5.11, 3.49, and 1.74 MPa for C_6F_{14}, C_5F_{12}, C_4F_{10}, and C_3F_8, respectively. Calculating the MI for these thresholds resulted in values of 6.2, 4.6, 3.1, and 1.6, respectively [56]. For comparison, the MI corresponding to 80 % vaporization observed in our experiment is 0.24 for C_3F_8 droplets and 0.94 for those containing C_4F_{10}. While the values obtained by Li et al. are notably higher than those measured in our study, our thresholds remain consistent with data published elsewhere [22,46]. The difference between our study and that of Li et al. can be explained by their use of a transducer centered at 40 MHz for signal recording which aligns with the vaporization of very small droplets. Indeed, the resonance frequency of the resulting bubble inversely correlates with its size [15]. Besides, smaller droplets require higher vaporization pressures to undergo vaporization [25,26]. In a previous study, Rojas et al. demonstrated that vaporization threshold is higher *in vivo* than *in vitro* [57]. Similar trend was observed in our *in vivo* BBB opening experiments using both C_3F_8 and C_4F_{10} NDs. ND activation was achieved at an MI that is above the vaporization threshold observed *in vitro*. The vaporization threshold of droplets was found to be inversely proportional to the size of the tube constraining the suspension and the surrounding viscosity [57]. Although our single-tube microcellulose model is far from reproducing the complexity of the cerebral vascular network, our results also align with observations by Lin et al., who demonstrated that the contrast enhancement induced by ultrasonic vaporization of NDs in a tube was more than an order of magnitude lower than in a free environment [58]. Probable causes of this phenomenon include changes in the surface tension and viscosity of the surrounding medium when it is constrained. An improvement on our *in vitro* model would be to set up a set of microtubes of different sizes and dilute the droplets in a medium with a viscosity close to that of blood.

Experiments to determine the acoustic vaporization threshold of NDs were conducted using a setup identical to that employed in the study by Wu et al. [22]. While the same vaporization threshold was identified for C_3F_8 in both studies, a lower threshold was observed in their investigation for C_4F_{10} (750 kPa) [22]. It is crucial to note a difference between the studies: the technique used for droplet condensation varies. Wu et al. condensed their droplets by immersing the bubble vial in an isopropanol bath cooled with dry ice to temperatures between −8 °C and − 13 °C. The pressure within the vial was manually increased by pushing air into it with a syringe until a visual change in the suspension's appearance was observed. This method enabled a gradual increase in flask pressure, whereas in our protocol, the pressure was elevated more abruptly. Refining the droplet manufacturing protocol between the two studies resulted in enhanced droplet stability and increased reproducibility. This optimized condensation process could potentially reduce the occurrence of "large" droplets with inadequate condensation in the suspension. Given that larger droplets vaporize more easily than smaller ones, a plausible hypothesis to explain the observed differences is that a higher proportion of larger droplets are present in the suspension studied by Wu et al. compared to ours. Another explanation could be that when pressurizing with air, containing oxygen, some NDs could soak up oxygen leading to droplets easier to vaporize.

3.3. *In vivo BBB opening using FUS and ND suspensions*

ND suspensions were evaluated *in vivo* for their ability to open the BBB. Fig. 8 depicts T_1-weighted contrast MRI images acquired for C_3F_8 NDs and C_4F_{10} NDs for each of the explored ultrasound sequences. Only one MRI by sequence is displayed in the figure. Following ND injections, contrast enhancement becomes visible on the MRI image along the ultrasound beam path only if the BBB has been permeabilized.

C_3F_8 ND demonstrated efficacy in permeabilizing the BBB, with an opening threshold observed between 400 and 600 kPa, corresponding to a MI ranging from 0.3 to 0.5 for the three treated mice. Drawing from these findings, we developed a sequence capable of permeabilizing the entire brain of the animals at specified pressures (500 kPa for S2 sequence and 600 kPa for S3). Both sequences successfully disrupted the entire brain. However, T_2-weighted MRI conducted 48 h after ultrasound treatment revealed that the 600 kPa sequence (S3) led to hemorrhages in the animals' brains, whereas no damage was observed in animals treated at 500 kPa (S2). As shown on the MRI acquisitions, the presence of vascular damage is identifiable after sacrifice by gross pathology and histology for animals that were exposed to a pressure of 600 kPa (supplementary fig. 2) and no damage was observed in animals subjected to a pressure of 500 kPa. Based on our *in vitro* characterization, broadband noise was measured for C_3F_8 ND starting at 550 kPa. This measurments aligns with the damage observed *in vivo* above this pressure. For C_3F_8 NDs, the cavitation results obtained *in vitro* are perfectly in line with the data observed in our *in vivo* experiments. Following ND vaporization, stable cavitation ($2f_0$) was detected at pressures in the 400–500 kPa range. These stable cavitation events were accompanied by acoustic signatures at $1.5f_0$, precursors to inertial cavitation. In our *in vivo* data, we observe safe, effective openings at these pressures (sequences S1 and S2). However, at a higher pressure of 600 kPa (S3), damage is observed in the brains of rodents (edema present 48 h after opening). This PNP corresponds to the appearance of broadband noise *in vitro* (inertial cavitation). Our *in vitro* results perfectly predict these observations. These results show the interest and necessity of monitoring these cavitation events, in order to preserve the bubble oscillation regime in a state that allows opening of the BBB without inducing damage.

This is a limitation of our study, in which cavitation data could not be measured *in vivo*. Indeed, the continuous scanning sequences presented in this work require the implementation of technological solutions (high-volume data storage and ultra-fast data processing) on which we are currently working. Our group has just published an *in vivo* study in which we successfully implemented ultrafast monitoring by receiving and analyzing signals from microbubbles on an FPGA board in less than 100 μs [59]. The next step will be to evaluate this ultrafast cavitation monitoring approach on continuously scanned ultrasound sequences.

Concerning the sham sequence (C_3F_8 ND and MRI contrast agent injection without FUS), no change was observed after the procedure:

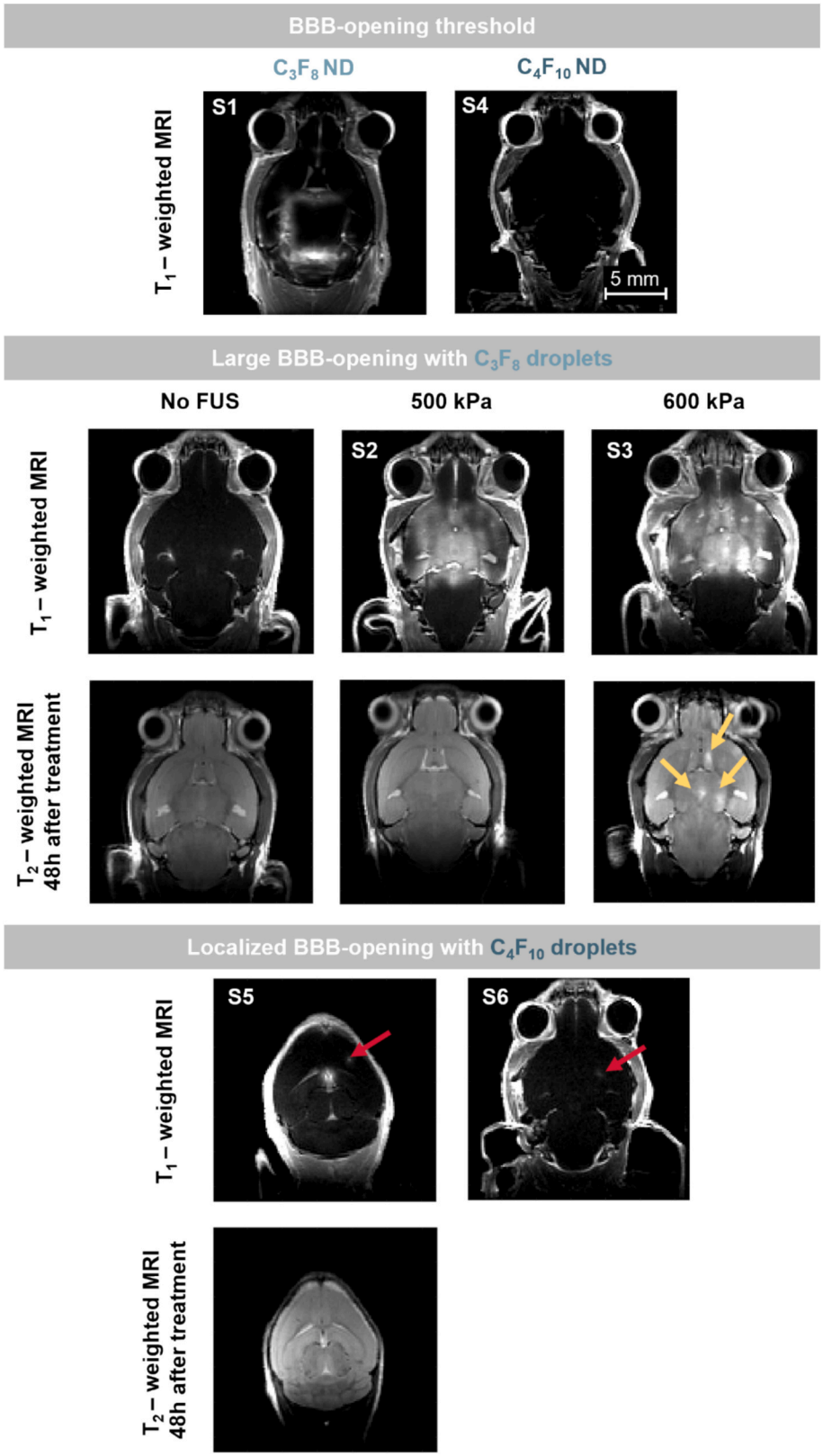

Fig. 8. FUS BBB opening in mice using nanodroplets: T_1-weighted MRI images immediately after the procedure; T_2-weighted MRI images 48 h after the procedure. Gadolinium contrast uptake is indicated by arrows for T_1-weighted MRI of S5 and S6 sequences. Damages observed in T2-weighted MRI are indicated by arrows.

neither BBB permeabilization (T_1-weighted MRI), nor damage observed 48 h after the experiment (T_2-weighted MRI).

In the case of C_4F_{10} ND droplets, the S4 sequence (from 400 to 1000 kPa) failed to permeabilize the BBB in the two treated animals. However, the S5 sequence (spot sequence) proved effective, with an MI of 1.2 for the vaporization pulse at 1500 kPa and 0.5 for the cavitation pulse at 600 kPa. The opening, though not highly intense, was very localized (sphere 0.4 mm × 0.4 mm × 0.4 mm) and visible on one or two MRI slice planes. This opening occurred only at the maximum pressure (probe focal point). No hemorrhage or edema were observed 48 h after the experiment on T_2-weighted images, as depicted in Fig. 8. The S6 sequence exhibited similar tiny localized permeabilization of the BBB.

For C_4F_{10} NDs, the pressures required for BBB opening *in vivo* (1.5 MPa) are much higher than the pressure required for vaporization *in vitro* (of the order of 1 MPa). It should be noted that the number of vaporization events observed under the *in vitro* microscope on C_4F_{10} NDs is much lower than those observed with C_3F_8 NDs. It is therefore possible that a small quantity of C_4F_{10} NDs is vaporized at 1 MPa *in vivo*, but that this small number is not sufficient to induce effective opening of the BBB. Beyond the thresholds of vaporization and stable, inertial cavitation, it might be interesting in a future study to correlate the number of ADVs observed *in vitro* with the intensity of BBB opening.

MRI sequences presented here allow for qualitative observation of the images, with signal intensity influenced by various experimental parameters (mouse morphology, injection quality, positioning of the therapeutic transducer, and antenna on the animal). Comparisons between mice are not viable due to these variations. However, within the same mouse, it is possible to determine whether permeabilization has occurred. Additionally, for scanning sequences drawing a square, where the transmitted PNP along the sides differ, qualitative analysis can detect an opening threshold.

There are very few studies on BBB opening using C_4F_{10} and C_3F_8 NDs in the literature—only two, to the best of our knowledge [22,32].

These publications originate from a collaboration between the teams of Elisa Konofagou (Columbia University) and Paul Dayton (University of North Carolina at Chapel Hill) [22,32]. In 2013, C_4F_{10} ND induced BBB permeabilization in mice at 600 kPa ($f_0 = 1.5$ MHz) [32]. In 2018, Wu et al. reported BBB openings in mice induced by droplets at a PNP of 900 kPa for C_4F_{10} and 450 kPa for C_3F_8 ($f_0 = 1.5$ MHz) [22]. The stated PNP were calculated by estimating 18 % skull attenuation at 1.5 MHz, corresponding to MI of 0.7 (900 kPa), 0.5 (600 kPa), and 0.4 (450 kPa). In our experiments, C_3F_8 ND induced BBB permeabilization at the same threshold as identified by Wu et al. (with an MI between 0.3 and 0.5). Conversely, in our experiments, C_4F_{10} ND permeabilized the BBB at an MI of 1.2. C_4F_{10} NDs remain compelling due to their efficient condensation, relative stability, and ease of use.

BBB opening for C_3F_8 NDs was achieved at an MI that is above the vaporization threshold observed *in vitro* but below the broadband noise detection level also noted *in vitro*. For C_4F_{10} NDs, BBB opening was achieved with an MI exceeding the vaporization threshold observed *in vitro*. The results from both *in vitro* and *in vivo* experiments in this study are consistent.

As demonstrated by the results of the S6 sequence, vaporization of the droplets alone may be sufficient for BBB permeabilization. Yet, C_4F_{10} droplets encapsulating Nile blue has been acoustically vaporized in rat brain to deliver the dye with a sub-millimeter precision ($f_0 = 1.66$ MHz, PNP = 1.74 MPa, PRF = 1 Hz) through an intact BBB in rats [46]. Indeed, Nile blue is a lipophilic agent with a molecular weight under 400 Da, making it one of the few molecules capable of crossing an intact BBB [46]. BBB integrity was assessed in this study by assessing under identical condition NDs encapsulating agents that do not cross an intact BBB (Nile Red and Quantum Dots of 5 nm diameter). These agents were not delivered, confirming that the BBB remained intact and that in this study, droplet vaporization alone was not sufficient to permeabilize the BBB [46]. However, the MI value employed in this study is higher than the one that achieve BBB opening in our study (1.4 *vs* 1.2).

Our findings indicate that the ultrasound sequence transmitted can be precisely adjusted to deliver an initial ultrasonic burst capable of vaporizing the droplets, followed by a second burst at a lower pressure to allow the microbubbles formed to oscillate without causing tissue damage.

In our preclinical study, a frequency of 1.5 MHz was chosen as it is highly suitable for opening the BBB in rodents, avoiding the beam widening of lower frequencies, which isn't ideal for the small mouse brain [60] and standing waves [61] induced by multiple reflections at the brain/skull interface. For clinical BBB opening, low central frequencies are typically used to penetrate the human skull. Most procedures employ a frequency of 220 kHz [8,62], though frequencies of 500 kHz [63] and 1 MHz [6,7,64] are also used. In the latter case, ultrasound is applied post-surgery, after skull incision. However, previous work reported that acoustic droplet vaporization (ADV) threshold increases with frequency [65,66]. It is therefore expected that the ADV threshold will be even lower when using a clinical ultrasound device. This hypothesis, which will have to be validated in large animals, would be highly beneficial, as the application of wide opening sequences with ND C_3F_8 or very precise sequences with ND C_4F_{10} could be performed in the patient at lower acoustic pressure in agreement with safety standards.

As an example, an adaptive sequence based on frequency variation was tested on chicken livers *ex vivo* using two different transducers: one with a high frequency (5 MHz) and another with adjustable low frequencies (850, 250, and 80 kHz) [67]. This approach demonstrated that ND vaporization (5 MHz, 4.1 MPa, 2 cycles), followed by microbubble activation (80 kHz, MI = 0.9 *i.e.* PNP = 250 kPa, PRF = 33 Hz, duration = 1 s), successfully achieved tissue ablation while maintaining the MI within the FDA-recommended limit of 0.9 for such applications [67].

The same number of cycles was applied in each of the *in vitro* conditions. This same number of cycles was also applied *in vivo* in the S5 and S6 single spot sequences to remain consistent with *in vitro* measurements. However, it was necessary to change this parameter in the continuous scan sequence. This type of sequence has been developed in the laboratory for over 10 years [41,68], and enables a molecule to be delivered over a large brain volume. Although the duty cycles (91 % for S1 and S4) and 69 % (for S2 and S3) are impressive, it should be borne in mind that the probe moves continuously over the animal's head at a speed of 10 mm/s. Thus, an area of 1 mm (corresponding to the focal spot) will be insonified for a maximum of 100 ms. In detail, as the trajectory used for sequences S1 and S4 is repeated every 2.3 s, the effective cycle ratio per zone treated is 4.3 % (100 × 0.1/2.3). For sequences S2 and S3, the trajectory is repeated every 5 s, giving an effective cycle ratio per zone treated of 2 % (100 × 0.1/5).

Pulse length has little influence on the vaporization threshold [21]. Few studies report that this ADV threshold is slightly reduced when the number of cycles is increased [69,70]. On the other hand, increasing the number of cycles will activate a greater number of droplets circulating in the sonicated volume, and thus increase the therapeutic effect. The choice of 50 cycles for sequences S5 and S6 was dictated by a desire not to induce damage in the animal. Indeed, the acoustic pressure of 1.5 MPa is already high, and it seemed more prudent to use a reasonable number of cycles whose efficacy had already been demonstrated by our *in vitro* results. Increasing the number of cycles for C_4F_{10} NDs activation (or the PRF) could be a relevant option to improve drug delivery to the brain, while remaining highly targeted.

In summary, based on our initial *in vivo* findings, it appears that C_3F_8 NDs are well-suited for achieving widespread permeabilization of the BBB at lower pressures, making them suitable for conditions such as genetic diseases and Alzheimer's. On the other hand, C_4F_{10} NDs might be employed for highly precise openings, making them applicable to the treatment of localized pathologies, such as brain metastases.

4. Conclusion and perspectives

We have produced and analyzed two low-boiling point

perfluorocarbon nanodroplets containing either C_3F_8 or C_4F_{10}. The challenge involved designing droplets that remained sufficiently stable in solution and in circulation, while still being vaporizable within a specific window of ultrasound parameters that avoided side effects for patients. We observed droplets morphology and structure through TEM and cryo-TEM, highlighting the coexistence of liposomes and droplets with suspended lipids. Moreover, *in vitro* acoustic characterization was performed, focusing on vaporization thresholds and studying the acoustic signature of vaporized bubbles, crucial for their validation. On one hand, C_3F_8 NDs exhibited vaporization at MI = 0.24, and emitted signals at $2\,f_0$ and $1.5\,f_0$ from MI = 0.37 onwards, while broadband noise was measured starting from MI = 0.45. On the other hand, C_4F_{10} NDs vaporized at MI = 0.94 and emitted signals at $2\,f_0$ from MI = 0.53 and $1.5\,f_0$ from MI = 0.73, while broadband noise was detected strating from MI = 0.78. Finally, the efficacy of C_3F_8 and C_4F_{10} nanodroplets in permeabilizing the BBB was validated *in vivo* in mice, demonstrating the distinct applicability of each perfluorocarbon: C_3F_8 for achieving a large, comprehensive opening, and C_4F_{10} for achieving a precise, targeted opening.

Funding sources

This work was funded by the ANR DROPMUT (grant ANR-19-CE19-0011), the IRP SONATA supported by the CNRS INSIS and has been supported by the Fondation ARC pour la recherche sur le cancer. The present work has benefited from the core facilities of Imagerie-Gif, (http://www.i2bc.paris-saclay.fr), member of IBiSA (http://www.ibisa.net), supported by "France-BioImaging" (ANR-10-INBS-04-01), and the Labex "Saclay Plant Science" (ANR-11-IDEX-0003-02). This work also benefited from the CryoEM platform of I2BC, supported by the French Infrastructure for Integrated Structural Biology (FRISBI) (ANR-10-INBS-05-05).

Supplementary data to this article can be found online at https://doi.org/10.1016/j.jconrel.2024.10.023.

CRediT authorship contribution statement

Ambre Dauba: Writing – review & editing, Writing – original draft, Investigation, Formal analysis, Data curation. **Claire Spitzlei:** Writing – review & editing, Investigation. **Kathlyne Jayne B. Bautista:** Writing – review & editing, Investigation. **Laurène Jourdain:** Investigation, Formal analysis. **Erwan Selingue:** Writing – review & editing, Investigation. **Kelly E. VanTreeck:** Writing – review & editing, Investigation. **Jacob A. Mattern:** Writing – review & editing, Investigation. **Caroline Denis:** Investigation. **Malika Ouldali:** Writing – review & editing, Investigation. **Ana-Andreea Arteni:** Writing – review & editing, Investigation. **Charles Truillet:** Writing – review & editing, Methodology, Formal analysis. **Benoit Larrat:** Writing – review & editing, Methodology. **James Tsuruta:** Writing – review & editing, Methodology. **Phillip G. Durham:** Writing – review & editing, Methodology. **Virginie Papadopoulou:** Writing – review & editing, Supervision, Funding acquisition. **Paul A. Dayton:** Writing – review & editing, Supervision, Funding acquisition. **Nicolas Tsapis:** Writing – review & editing, Supervision, Methodology, Funding acquisition, Conceptualization. **Anthony Novell:** Writing – review & editing, Supervision, Methodology, Investigation, Funding acquisition, Formal analysis, Data curation, Conceptualization.

Declaration of competing interest

P.A.D. declares inventorship on patents describing low boiling point nanodroplet technologies, some of which have been licensed to Triangle Biotechnology. P.A.D. declares he is a co-founder and board member for Triangle Biotechnology.

BL and AN are cofounders and stockholders of the company TheraSonic developing an ultrasound device for blood-brain barrier opening.

All other authors declare that they do not have any competing interest.

The figures used in this manuscript were partially generated using the Servier Medical Art image bank provided by Servier under a Creative Commons Attribution 3.0 Unported License (https://creativecommons.org/licenses/by/3.0/) and the BioRender.com website.

Data availability

Data will be made available on request.

Acknowledgements

We gratefully acknowledge the assistance of Magali Noiray and Julie Mougin (Institut Galien Paris-Saclay) with the Nanosight measurements. We also acknowledge Sébastien Mériaux (Neuropsin) for his help in processing the MRI images, and Brian Velasco (University of North Carolina at Chapel Hill) for nanodroplet preparation assistance.

References

[1] C.D. Arvanitis, G.B. Ferraro, R.K. Jain, The blood–brain barrier and blood–tumour barrier in brain tumours and metastases, Nat. Rev. Cancer 20 (1) (Jan. 2020) 26–41, https://doi.org/10.1038/s41568-019-0205-x.
[2] A. Burgess, K. Shah, O. Hough, K. Hynynen, Focused ultrasound-mediated drug delivery through the blood–brain barrier, Expert. Rev. Neurother. 15 (5) (May 2015) 477–491, https://doi.org/10.1586/14737175.2015.1028369.
[3] K. Hynynen, N. McDannold, N. Vykhodtseva, F.A. Jolesz, Noninvasive MR imaging–guided focal opening of the blood-brain barrier in rabbits, Radiology 220 (3) (Sep. 2001) 640–646, https://doi.org/10.1148/radiol.2202001804.
[4] A. Burgess, K. Hynynen, Microbubble-Assisted Ultrasound for Drug Delivery in the Brain and Central Nervous System, in: J.-M. Escoffre, A. Bouakaz (Eds.), Therapeutic Ultrasound, Advances in Experimental Medicine and Biology, vol. 880, Cham: Springer International Publishing, 2016, pp. 293–308, https://doi.org/10.1007/978-3-319-22536-4_16.
[5] Y. Meng, et al., Safety and efficacy of focused ultrasound induced blood-brain barrier opening, an integrative review of animal and human studies, J. Control. Release 309 (Sep. 2019) 25–36, https://doi.org/10.1016/j.jconrel.2019.07.023.
[6] A. Carpentier, et al., Clinical trial of blood-brain barrier disruption by pulsed ultrasound, Sci. Transl. Med. 8 (343) (Jun. 2016), https://doi.org/10.1126/scitranslmed.aaf6086, 343re2-343re2.
[7] A. Idbaih, et al., Safety and Feasibility of Repeated and Transient Blood–Brain Barrier Disruption by Pulsed Ultrasound in Patients with Recurrent Glioblastoma, Clin. Cancer Res. 25 (13) (Jul. 2019) 3793–3801, https://doi.org/10.1158/1078-0432.CCR-18-3643.
[8] N. Lipsman, et al., Blood–brain barrier opening in Alzheimer's disease using MR-guided focused ultrasound, Nat. Commun. 9 (1) (Dec. 2018) 2336, https://doi.org/10.1038/s41467-018-04529-6.
[9] I. Lentacker, I. De Cock, R. Deckers, S.C. De Smedt, C.T.W. Moonen, Understanding ultrasound induced sonoporation: definitions and underlying mechanisms, Adv. Drug Deliv. Rev. 72 (Jun. 2014) 49–64, https://doi.org/10.1016/j.addr.2013.11.008.
[10] S. Qin, C.F. Caskey, K.W. Ferrara, Ultrasound contrast microbubbles in imaging and therapy: physical principles and engineering, Phys. Med. Biol. 54 (6) (Mar. 2009) R27–R57, https://doi.org/10.1088/0031-9155/54/6/R01.
[11] H. Lee, et al., Microbubbles used for contrast enhanced ultrasound and theragnosis: a review of principles to applications, Biomed. Eng. Lett. 7 (2) (May 2017) 59–69, https://doi.org/10.1007/s13534-017-0016-5.
[12] A. Novell, et al., A new safety index based on intrapulse monitoring of ultra-harmonic cavitation during ultrasound-induced blood-brain barrier opening procedures, Sci. Rep. 10 (1) (Dec. 2020) 10088, https://doi.org/10.1038/s41598-020-66994-8.
[13] J.H. Hwang, J. Tu, A.A. Brayman, T.J. Matula, L.A. Crum, Correlation between inertial cavitation dose and endothelial cell damage in vivo, Ultrasound Med. Biol. 32 (10) (Oct. 2006) 1611–1619, https://doi.org/10.1016/j.ultrasmedbio.2006.07.016.
[14] A. Dauba, et al., Recent advances on ultrasound contrast agents for blood-brain barrier opening with focused ultrasound, Pharmaceutics 12 (11) (Nov. 2020) 1125, https://doi.org/10.3390/pharmaceutics12111125.
[15] K. Kooiman, H.J. Vos, M. Versluis, N. de Jong, Acoustic behavior of microbubbles and implications for drug delivery, Adv. Drug Deliv. Rev. 72 (Jun. 2014) 28–48, https://doi.org/10.1016/j.addr.2014.03.003.
[16] T. Boissenot, A. Bordat, E. Fattal, N. Tsapis, Ultrasound-triggered drug delivery for cancer treatment using drug delivery systems: from theoretical considerations to practical applications, J. Control. Release 241 (Nov. 2016) 144–163, https://doi.org/10.1016/j.jconrel.2016.09.026.
[17] J. Deprez, G. Lajoinie, Y. Engelen, S.C. De Smedt, I. Lentacker, Opening doors with ultrasound and microbubbles: beating biological barriers to promote drug delivery, Adv. Drug Deliv. Rev. 172 (May 2021) 9–36, https://doi.org/10.1016/j.addr.2021.02.015.

[18] N.A. Lapin, K. Gill, B.R. Shah, R. Chopra, Consistent opening of the blood brain barrier using focused ultrasound with constant intravenous infusion of microbubble agent, Sci. Rep. 10 (1) (Oct. 2020) 16546, https://doi.org/10.1038/s41598-020-73312-9.

[19] E. Stride, et al., Microbubble agents: new directions, Ultrasound Med. Biol. 46 (6) (Jun. 2020) 1326–1343, https://doi.org/10.1016/j.ultrasmedbio.2020.01.027.

[20] R. Gattegno, L. Arbel, N. Riess, H. Shinar, S. Katz, T. Ilovitsh, Enhanced capillary delivery with nanobubble-mediated blood-brain barrier opening and advanced high resolution vascular segmentation, J. Control. Release 369 (2024) 506–516.

[21] P.S. Sheeran, P.A. Dayton, Phase-change contrast agents for imaging and therapy, CPD 18 (15) (Mar. 2012) 2152–2165, https://doi.org/10.2174/138161212800099883.

[22] S.-Y. Wu, et al., Focused ultrasound-facilitated brain drug delivery using optimized nanodroplets: vaporization efficiency dictates large molecular delivery, Phys. Med. Biol. 63 (3) (Jan. 2018) 035002, https://doi.org/10.1088/1361-6560/aaa30d.

[23] A. Yildirim, N.T. Blum, A.P. Goodwin, Colloids, nanoparticles, and materials for imaging, delivery, ablation, and theranostics by focused ultrasound (FUS), Theranostics 9 (9) (2019) 2572–2594, https://doi.org/10.7150/thno.32424.

[24] P.S. Sheeran, P.A. Dayton, Improving the performance of phase-change perfluorocarbon droplets for medical ultrasonography: current Progress, challenges, and prospects, Scientifica 2014 (2014) 1–24, https://doi.org/10.1155/2014/579684.

[25] P.S. Sheeran, S. Luois, P.A. Dayton, T.O. Matsunaga, Formulation and acoustic studies of a new phase-shift agent for diagnostic and therapeutic ultrasound, Langmuir 27 (17) (Sep. 2011) 10412–10420, https://doi.org/10.1021/la2013705.

[26] H. Lea-Banks, M.A. O'Reilly, K. Hynynen, Ultrasound-responsive droplets for therapy: a review, J. Control. Release 293 (Jan. 2019) 144–154, https://doi.org/10.1016/j.jconrel.2018.11.028.

[27] P.S. Sheeran, K. Yoo, R. Williams, M. Yin, F.S. Foster, P.N. Burns, More than bubbles: creating phase-shift droplets from commercially available ultrasound contrast agents, Ultrasound Med. Biol. 43 (2) (Feb. 2017) 531–540, https://doi.org/10.1016/j.ultrasmedbio.2016.09.003.

[28] R. Song, et al., Cavitation-facilitated transmembrane permeability enhancement induced by acoustically vaporized nanodroplets, Ultrason. Sonochem. 79 (Nov. 2021) 105790, https://doi.org/10.1016/j.ultsonch.2021.105790.

[29] X. Zhang, et al., PEGylated PLGA-based phase shift nanodroplets combined with focused ultrasound for blood brain barrier opening in rats, Oncotarget 8, no. 24, Art. no. 24 (Jun. 2017), https://doi.org/10.18632/oncotarget.17155.

[30] K.A. Hallam, R.J. Nikolai, A. Jhunjhunwala, S.Y. Emelianov, Laser-Activated Perfluorocarbon Nanodroplets for Intracerebral Delivery and Imaging Via Blood–Brain Barrier Opening and Contrast- Enhanced Imaging, 2024.

[31] K.A. Hallam, E.M. Donnelly, A.B. Karpiouk, R.K. Hartman, S.Y. Emelianov, Laser-activated perfluorocarbon nanodroplets: a new tool for blood brain barrier opening, Biomed. Opt. Express 9 (9) (Sep. 2018) 4527–4538, https://doi.org/10.1364/BOE.9.004527.

[32] C.C. Chen, P.S. Sheeran, S.-Y. Wu, O.O. Olumolade, P.A. Dayton, E.E. Konofagou, Targeted drug delivery with focused ultrasound-induced blood-brain barrier opening using acoustically-activated nanodroplets, J. Control. Release 172 (3) (Dec. 2013) 795–804, https://doi.org/10.1016/j.jconrel.2013.09.025.

[33] S.G. Ting, H. Lea-Banks, K. Hynynen, Physical characterization to improve scalability and potential of anesthetic-loaded Nanodroplets, Pharmaceutics 15, no. 8, Art. no. 8 (Aug. 2023), https://doi.org/10.3390/pharmaceutics15082077.

[34] P.S. Sheeran, S.H. Luois, L.B. Mullin, T.O. Matsunaga, P.A. Dayton, Design of ultrasonically-activatable nanoparticles using low boiling point perfluorocarbons, Biomaterials 33 (11) (Apr. 2012) 3262–3269, https://doi.org/10.1016/j.biomaterials.2012.01.021.

[35] P.G. Durham, P.A. Dayton, Applications of sub-micron low-boiling point phase change contrast agents for ultrasound imaging and therapy, Curr. Opin. Colloid Interface Sci. 56 (Dec. 2021) 101498, https://doi.org/10.1016/j.cocis.2021.101498.

[36] S.M. Fix, A. Novell, Y. Yun, P.A. Dayton, C.B. Arena, An evaluation of the sonoporation potential of low-boiling point phase-change ultrasound contrast agents in vitro, J Ther Ultrasound 5 (1) (Dec. 2017) 7, https://doi.org/10.1186/s40349-017-0085-z.

[37] B. Carr, M. Wright, Nanoparticle Tracking Analysis (NTA) | Malvern Panalytical, Malvern Panalytical, 2015.

[38] "AccuSizer® SPOS Systems | Particle Characterization | USD | Entegris." Accessed: May 03, 2023. [Online]. Available: https://www.entegris.com/shop/en/USD/products/fluid-management/process-monitoring/particle-characterization/AccuSizer-SPOS-Systems/p/AccuSizerSPOSSystems.

[39] A. Dauba, et al., Evaluation of capacitive micromachined ultrasonic transducers for passive monitoring of microbubble-assisted ultrasound therapies, J. Acoust. Soc. Am. 148 (4) (Oct. 2020) 2248–2255, https://doi.org/10.1121/10.0002096.

[40] N. McDannold, Y. Zhang, N. Vykhodtseva, The Effects of Oxygen on Ultrasound-Induced Blood–Brain Barrier Disruption in Mice, Ultrasound Med. Biol. 43, no. 2, Art. no. 2 (Feb. 2017), https://doi.org/10.1016/j.ultrasmedbio.2016.09.019.

[41] G. Hugon, et al., [18F]2-Fluoro-2-deoxy-sorbitol PET imaging for quantitative monitoring of enhanced blood-brain barrier permeability induced by focused ultrasound, Pharmaceutics 13 (11) (Oct. 2021) 1752, https://doi.org/10.3390/pharmaceutics13111752.

[42] P.A. Mountford, W.S. Smith, M.A. Borden, Fluorocarbon Nanodrops as acoustic temperature probes, Langmuir 31 (39) (Oct. 2015) 10656–10663, https://doi.org/10.1021/acs.langmuir.5b02308.

[43] S.-Y. Yoon, et al., Novel animal model of spontaneous cerebral petechial hemorrhage using focused ultrasound in rats, Medicina 58 (7) (Jun. 2022) 881, https://doi.org/10.3390/medicina58070881.

[44] M.-S. Felix, et al., Ultrasound-mediated blood-brain barrier opening improves whole brain gene delivery in mice, Pharmaceutics 13 (8) (Aug. 2021) 1245, https://doi.org/10.3390/pharmaceutics13081245.

[45] P.G. Durham, J. Kim, K.M. Eltz, C.F. Caskey, P.A. Dayton, Polyvinyl alcohol Cryogels for acoustic characterization of phase-change contrast agents, Ultrasound Med. Biol. 48 (5) (May 2022) 954–960, https://doi.org/10.1016/j.ultrasmedbio.2022.01.007.

[46] H. Lea-Banks, K. Hynynen, Sub-millimetre precision of drug delivery in the brain from ultrasound-triggered nanodroplets, J. Control. Release 338 (Oct. 2021) 731–741, https://doi.org/10.1016/j.jconrel.2021.09.014.

[47] E. Amstad, J. Kohlbrecher, E. Müller, T. Schweizer, M. Textor, E. Reimhult, Triggered release from liposomes through magnetic actuation of Iron oxide nanoparticle containing membranes, Nano Lett. 11 (4) (Apr. 2011) 1664–1670, https://doi.org/10.1021/nl2001499.

[48] J. Owen, E. Stride, Technique for the characterization of phospholipid microbubbles coatings by transmission Electron microscopy, Ultrasound Med. Biol. 41 (12) (Dec. 2015) 3253–3258, https://doi.org/10.1016/j.ultrasmedbio.2015.07.024.

[49] M. Javadi, W.G. Pitt, D.M. Belnap, N.H. Tsosie, J.M. Hartley, Encapsulating Nanoemulsions inside eLiposomes for ultrasonic drug delivery, Langmuir 28 (41) (Oct. 2012) 14720–14729, https://doi.org/10.1021/la303464v.

[50] C. Hernandez, S. Gulati, G. Fioravanti, P.L. Stewart, A.A. Exner, Cryo-EM visualization of lipid and polymer-stabilized perfluorocarbon gas Nanobubbles - a step towards Nanobubble mediated drug delivery, Sci. Rep. 7 (1) (Oct. 2017) 13517, https://doi.org/10.1038/s41598-017-13741-1.

[51] D.V.B. Batchelor, et al., The influence of Nanobubble size and stability on ultrasound enhanced drug delivery, Langmuir 38 (45) (Nov. 2022) 13943–13954, https://doi.org/10.1021/acs.langmuir.2c02303.

[52] M.J. Moore, et al., The dance of the nanobubbles: detecting acoustic backscatter from sub-micron bubbles using ultra-high frequency acoustic microscopy, Nanoscale 12 (41) (2020) 21420–21428, https://doi.org/10.1039/D0NR05390B.

[53] A. Woodward, R.F. Mattrey, C. De Gracia Lux, Direct emulsification of stable superheated Perfluorobutane Nanodroplets by sonication: addressing the limitations of the microbubble condensation technique, Ultrasound Med. Biol. 50 (3) (Mar. 2024) 445–452, https://doi.org/10.1016/j.ultrasmedbio.2023.12.008.

[54] Q. Wu, et al., Investigation of the acoustic vaporization threshold of lipid-coated Perfluorobutane Nanodroplets using both high-speed optical imaging and acoustic methods, Ultrasound Med. Biol. 47 (7) (Jul. 2021) 1826–1843, https://doi.org/10.1016/j.ultrasmedbio.2021.02.019.

[55] Y.-S. Tung, J.J. Choi, B. Baseri, E.E. Konofagou, Identifying the inertial cavitation threshold and skull effects in a vessel phantom using focused ultrasound and microbubbles, Ultrasound Med. Biol. 36 (5) (May 2010) 840–852, https://doi.org/10.1016/j.ultrasmedbio.2010.02.009.

[56] D.S. Li, S. Schneewind, M. Bruce, Z. Khaing, M. O'Donnell, L. Pozzo, Spontaneous nucleation of stable perfluorocarbon emulsions for ultrasound contrast agents, Nano Lett. 19 (1) (Jan. 2019) 173–181, https://doi.org/10.1021/acs.nanolett.8b03585.

[57] J.D. Rojas, M.A. Borden, P.A. Dayton, Effect of hydrostatic pressure, boundary constraints and viscosity on the vaporization threshold of low-boiling-point phase-change contrast agents, Ultrasound Med. Biol. 45 (4) (Apr. 2019) 968–979, https://doi.org/10.1016/j.ultrasmedbio.2018.11.006.

[58] S. Lin, G. Zhang, C.H. Leow, M.-X. Tang, Effects of microchannel confinement on acoustic vaporisation of ultrasound phase change contrast agents, Phys. Med. Biol. 62 (17) (Aug. 2017) 6884–6898, https://doi.org/10.1088/1361-6560/aa8076.

[59] C. Cornu, et al., CMUT for ultrafast passive cavitation detection during ultrasound-induced blood-brain barrier disruption: proof of concept study, Phys. Med. Biol. 69 (20) (2024) 205015, https://doi.org/10.1088/1361-6560/ad8334.

[60] P. Mondou, S. Mériaux, F. Nageotte, J. Vappou, A. Novell, B. Larrat, State of the art on microbubble cavitation monitoring and feedback control for blood-brain-barrier opening using focused ultrasound, Phys. Med. Biol. 68 (18) (2023), https://doi.org/10.1088/1361-6560/ace23e.

[61] M.A. O'Reilly, Y. Huang, K. Hynynen, The impact of standing wave effects on transcranial focused ultrasound disruption of the blood-brain barrier in a rat model, Phys. Med. Biol. 55 (18) (Sep. 2010) 5251–5267, https://doi.org/10.1088/0031-9155/55/18/001.

[62] Y. Meng, et al., Putaminal recombinant Glucocerebrosidase delivery with magnetic resonance – guided focused ultrasound in Parkinson's disease: a phase I study, Mov. Disord. 37, no. 10, Art. no. 10 (Oct. 2022), https://doi.org/10.1002/mds.29190.

[63] K.-T. Chen, et al., Neuronavigation-guided focused ultrasound for transcranial blood-brain barrier opening and immunostimulation in brain tumors, Sci. Adv. 7, no. 6, Art. no. 6 (Feb. 2021), https://doi.org/10.1126/sciadv.abd0772.

[64] S. Epelbaum, et al., Pilot study of repeated blood-brain barrier disruption in patients with mild Alzheimer's disease with an implantable ultrasound device, Alz Res Therapy 14, no. 1, Art. no. 1 (Mar. 2022), https://doi.org/10.1186/s13195-022-00981-1.

[65] M. Aliabouzar, K.N. Kumar, K. Sarkar, Effects of droplet size and perfluorocarbon boiling point on the frequency dependence of acoustic vaporization threshold, J. Acoust. Soc. Am. 145 (2) (Feb. 2019) 1105–1116, https://doi.org/10.1121/1.5091781.

[66] P.S. Sheeran, T.O. Matsunaga, P.A. Dayton, Phase-transition thresholds and vaporization phenomena for ultrasound phase-change nanoemulsions assessed via high-speed optical microscopy, Phys. Med. Biol. 58 (13) (Jul. 2013) 4513–4534, https://doi.org/10.1088/0031-9155/58/13/4513.

[67] B. Glickstein, Nanodroplet-mediated low-energy mechanical ultrasound surgery, Ultrasound in Medicine 48 (7) (2022).

[68] V.L. Tran, et al., Impact of blood-brain barrier permeabilization induced by ultrasound associated to microbubbles on the brain delivery and kinetics of cetuximab: an immunoPET study using 89Zr-cetuximab, J. Control. Release 328 (Dec. 2020) 304–312, https://doi.org/10.1016/j.jconrel.2020.08.047.
[69] A. Lo, O. Kripfgans, P. Carson, E. Rothman, J. Fowlkes, Acoustic droplet vaporization threshold: effects of pulse duration and contrast agent, IEEE Trans. Ultrason., Ferroelect., Freq. Contr. 54 (5) (May 2007) 933–946, https://doi.org/10.1109/TUFFC.2007.339.
[70] N. Reznik, R. Williams, P.N. Burns, Investigation of vaporized submicron perfluorocarbon droplets as an ultrasound contrast agent, Ultrasound Med. Biol. 37 (8) (Aug. 2011) 1271–1279, https://doi.org/10.1016/j.ultrasmedbio.2011.05.001.